Article

Metallogenic Difference between the Late Aptian Nansu and Aishan Pluton in Jiaodong: Constraints from In Situ Apatite Elemental and Nd Isotopic Composition

Kexin Li [1], Liqiang Yang [1,2,3,*], Lei Ju [4] and Dong Xie [1]

1 State Key Laboratory of Geological Processes and Mineral Resources, Frontiers Science Center for Deep-Time Digital Earth, China University of Geosciences, Beijing 100083, China; likx0135@163.com (K.L.); dongxie@email.cugb.edu.cn (D.X.)
2 Ministry of Natural Resources Key Laboratory of Gold Mineralization Processes and Resources Utilization, Key Laboratory of Metallogenic-Geologic Processes and Comprehensive Utilization of Minerals Resources in Shandong Province, Shandong Institute of Geological Sciences, Jinan 250013, China
3 Institute of Geological Research, Shandong Gold Group Co., Ltd., Jinan 250101, China
4 Kunlun Digital Technology Co., Ltd., Beijing 100007, China; julei0220@163.com
* Correspondence: lqyang@cugb.edu.cn

Abstract: A series of Mo-polymetallic deposits have been developed in the Jiaodong Peninsula. Notably, these Mo-dominant deposits formed essentially during the same period as the well-known world-class Au deposits in this area, hinting at a potentially unique geological correlation between them. Therefore, conducting thorough research on Mo deposits in Jiaodong holds significant importance in exploring the area's controlling factors of Mesozoic metal endowments. To reveal the petrogenesis and metallogenic potentials of Mo-fertile and ore-barren granitoid, apatite grains from the Late Aptian Nansu granodiorite and Aishan monzogranite are investigated in this study. Detailed petrographical observations, combined with in situ analysis of electron probe micro-analyzer (EPMA) and Laser-ablation inductively coupled plasma mass spectrometry (LA-ICP-MS), have been conducted on apatite grains from the Nansu and Aishan plutons. This comprehensive analysis, encompassing both major and trace elements as well as isotopic characteristics of apatite, aims to elucidate the metallogenic differences within the late Early Cretaceous granitoids of Jiaodong. The results reveal that the apatite grains across all samples belong to fluorapatites, suggesting their magmatic origin. Additionally, chondrite-normalized rare earth element (REE) patterns of apatites in ore-fertile and ore-barren granitoids exhibit a "right-leaning" trend, characterized by relative enrichments in light REEs and depletions in heavy REEs. Both the Nansu and Aishan plutons exhibit moderately negative Eu anomalies (with averages δEu values of 0.44 and 0.51, respectively), along with slightly positive Ce anomalies (averaging δCe values of 1.08 and 1.11, respectively). A negative correlation is observed between their δEu and δCe values, indicating that the parental magmas of ore-fertile and ore-barren granitoids were formed in a relatively oxidizing environment. The calculated apatite OH contents for the Nansu pluton range from 0.26 to 1.38, while those for the Aishan pluton vary between 0.24 and 1.51, indicating comparable melt H_2O abundances. Consequently, the results suggest that neither the oxygen fugacities nor the water contents of the parental magma can account for the metallogenic differences between Nansu and Aishan plutons. The apatite in the Nansu pluton exhibits a higher Ce/Pb ratio and a relatively lower Th/U ratio, indicating the involvement of a greater volume of fluids in the magmatic evolution process of this ore-bearing granitoid. Apatite grains sourced from the Nansu and Aishan plutons exhibit $\varepsilon_{Nd}(t)$ values ranging from −16.63 to −17.61 (t = 115.7 Ma) and −17.86 to −20.86 (t = 116.8 Ma), respectively. These results suggest that their parental magmas primarily originated from the partial melting of Precambrian metamorphic basement rocks within the North China Craton, with a minor contribution from mantle-derived materials. Additionally, the presence of mafic microgranular enclaves in both the Nansu and Aishan plutons indicates that both have undergone magma mixing processes. The binary diagrams plotting the ratios of Ba/Th, Sr/Th, and U/Th against La/Sm demonstrate that apatite grains of ore-fertile granitoid exhibit a distinct trend towards sediment melting. This suggests the potential incorporation of sedimentary materials, particularly those rich in molybdenum, into the magmatic source of the Nansu pluton, ultimately leading to the occurrence of molybdenum mineralization.

1. Introduction

China is abundantly endowed with molybdenum resources. As of 2021, its proven molybdenum resource reserves stand at 830 Mt [1], representing over 51% of the global molybdenum reserves, making it the country with the most extensive molybdenum resources worldwide. Based on the temporal and spatial distribution of molybdenum deposits and the metallogenic tectonic setting in China, six major molybdenum metallogenic belts have been identified. These include the East Qinling–Dabie molybdenum metallogenic belt, the Xing–Meng molybdenum metallogenic belt, the middle and lower Yangtze River molybdenum metallogenic belt, the South China molybdenum metallogenic belt, the Qinghai–Tibet Plateau molybdenum metallogenic belt, and the Tianshan–Beishan molybdenum metallogenic belt [2]. The Jiaodong Peninsula stands as the most crucial gold mineralization area in China. Apart from gold deposits, the Late Mesozoic era also witnessed the formation of nonferrous polymetallic mineral deposits and occurrences encompassing a range of metals such as Cu, Mo, W, Pb, Zn, and Ag [3–5]. The Late Mesozoic Mo-polymetallic deposits and occurrences were sporadically distributed in the Jiaodong Peninsula, with the Late Jurassic Xingjiashan porphyry-skarn Mo deposit (the amount of molybdenum resources is 589,000 t, with an average grade of 0.12%), and the Early Cretaceous Shangjiazhuang porphyry Mo-Cu deposit (molybdenum resources are 55,000 t, with an average grade of 0.066%), the Kongxintou Mo-Cu deposit (molybdenum resources content 5271 t, average grade 0.13%), the Lengjia Mo deposit and the Nansu Mo occurrence [5–8]. At present, there are relatively few studies on molybdenum deposits in Jiaodong. Previous studies have systematically studied the timing limit of Mesozoic molybdenum mineralization in Jiaodong [3,4,6]. The metallogenic characteristics, ore-forming mechanism and geodynamic background, and ore-forming process of the late Jurassic Xingjiashan large porphyry-skarn Mo deposit and the late Early Cretaceous Shangjiazhuang porphyry Mo-Cu deposit are discussed [3–6,8]. However, compared with the main molybdenum metallogenic belts in China, the distribution range of molybdenum deposits in Jiaodong is limited, and the scale of deposits (mineralization) is quite different. The controlling factors of the Mo deposit scale in Jiaodong are still unclear, and the factors controlling the metallogenic difference of Mo deposits in the late Early Cretaceous need to be studied urgently.

Apatite, chemically represented as $Ca_5(PO_4)_3(F, Cl, OH)$, is a commonly encountered accessory mineral that is ubiquitously found in a diverse array of magmatic rocks, their hydrothermal alteration products [9–13], as well as metamorphic rocks [14–16]. Apatite is highly regarded as an effective indicator of petrogenesis and metallogenic potential due to its robust resistance to weathering and its chemical composition's sensitivity to crystallization environments and their variations [17–19]. Many major and trace elements, such as Fe, Mn, F, Cl, Sr, Th, U, and REEs, can be incorporated into the apatite lattice by isotropic substitution. The contents of these elements in apatite are closely related to parental magma composition, water content, oxygen fugacity, and magmatic differentiation [11,17,20–28]. Apatite microanalysis technology offers an efficient means for studying granite genesis and mineralization. This method can unveil crucial information about magmatic processes that may remain undetected through whole-rock geochemical research methods. Additionally, it enables the distinction of rock types, traces the nature of magmatic sources and magmatic compositions, reveals intricate magmatic evolution and petrologic processes, and facilitates the deduction of redox states in magmas [11,17,19–21,28–33]. Therefore, in this paper, apatites from the Late Aptian ore-fertile Nansu granodiorite and ore-barren Aishan monzogranite in Jiaodong are taken as the research objectives. The in situ elements and Nd isotope of apatite were analyzed, and the differences between the ore-fertile and ore-barren granitoids were compared to explore the key factors controlling the mineralization of the

late Early Cretaceous pluton in Jiaodong. The results indicate that the difference in the magmatic source is one of the most important reasons for the metallogenic difference of the late Early Cretaceous pluton in Jiaodong. Therefore, this paper holds that the source of magma serves as the critical determinant in controlling the mineralization of the late Early Cretaceous rock mass in Jiaodong.

2. Geological Background

2.1. Regional Geology

The Jiaodong Peninsula, situated at the southeastern fringe of the North China Craton, is delimited by the Tanlu fault in the west, the Pacific plate subduction zone in the east, and the Sulu–Dabie ultrahigh-pressure metamorphic zone in the south. The Jiaodong Peninsula is divided into two parts by the Wulian–Yantai fault: the Sulu orogenic belt in the eastern part and the Jiaobei terrane in the western section. The ultrahigh-pressure metamorphic rocks in the Sulu orogenic belt are mainly composed of Neoproterozoic ultrahigh-pressure metamorphic rocks, followed by Coesite-bearing eclogite, schist, and quartzite [34–39]. The Jiaobei terrane is located in the northwest of the Jiaodong Peninsula, including the Jiaobei uplift in the north and the Jiaolai basin in the south. It is mainly composed of Precambrian metamorphic basement and Mesozoic granite. More than 90% of the proven gold reserves in the Jiaodong area are located in the Jiaobei uplift [40–45]. The Mesozoic witnessed intense magmatic activity in the Jiaodong area, resulting in the widespread distribution of intrusive rocks. In this area, forty-two plutons with certain scales can be identified [46]. The intrusive rocks of the Mesozoic era in Jiaodong can be categorized into four stages: Late Triassic post-collision granite (215–205 Ma), Late Jurassic calc-alkaline granite (165–150 Ma), Middle Early Cretaceous high-K calc-alkaline granite (132–123 Ma), and Late Early Cretaceous alkaline granite (125–90 Ma) [43,47–51]. The majority of these age data determinations are based on SHRIMP zircon U-Pb and LA-ICP-MS zircon U-Pb. The Early Cretaceous granite is the commonest. The Late Triassic post-collision granite is formed by the northward subduction of the Triassic Yangtze Craton to the North China Craton. The subduction of the Paleo-Pacific plate at ~240–130 Ma led to the delamination and thinning of the lithosphere of the North China Craton, the upwelling of the asthenosphere, the increase of the thermal gradient, and the development of extensive magmatic activities [52,53]. Large-scale gold mineralization was developed in the Jiaodong area at ca. 120 Ma [44,47,54–57], with a large number of gold deposits hosted by the Mesozoic granitoids.

In addition to gold mineralization, Cu, Mo, W, Pb, Zn, and other polymetallic mineralization also developed during the Mesozoic period in the Jiaodong area. Molybdenum mineralization is mainly distributed in Fushan, Qixia, Muping, and Rongcheng of Jiaodong gold province (Figure 1) but mainly distributed in Qixia-Penglai-Fushan gold-polymetallic metallogenic area in the middle of Jiaodong Peninsula. Two main stages of molybdenum mineralization occurred in the Mesozoic in the Jiaodong Peninsula, including the Late Jurassic (160–150 Ma) and the Late Early Cretaceous (120–110 Ma). There is only one deposit in the Late Jurassic molybdenum mineralization, namely the Xingjiashan porphyry-skarn Mo-W deposit, which is the only large-scale porphyry-skarn deposit in Jiaodong Peninsula. The Early Cretaceous molybdenum mineralization is widely distributed in the Jiaodong Peninsula, ranging from medium-sized to small-sized and mineral occurrences, including the Shangjiazhuang porphyry Mo-Cu deposit, the Kongxintou porphyry-skarn Mo deposit, the Lengjia skarn Mo deposit and the Nansu molybdenum mineral occurrence [37,58–60]. The Mo-related rocks in Jiaodong are dominated by granodiorite and biotite granite, which is genetically related to the non-ferrous metal mineralization in this area. The formation of non-ferrous metal deposits in the Jiaodong area is closely related to favorable wall rock conditions, metallogenic tectonic settings, and late Early Cretaceous magmatic activities, among which molybdenum deposits are more closely related to magmatic rocks [61].
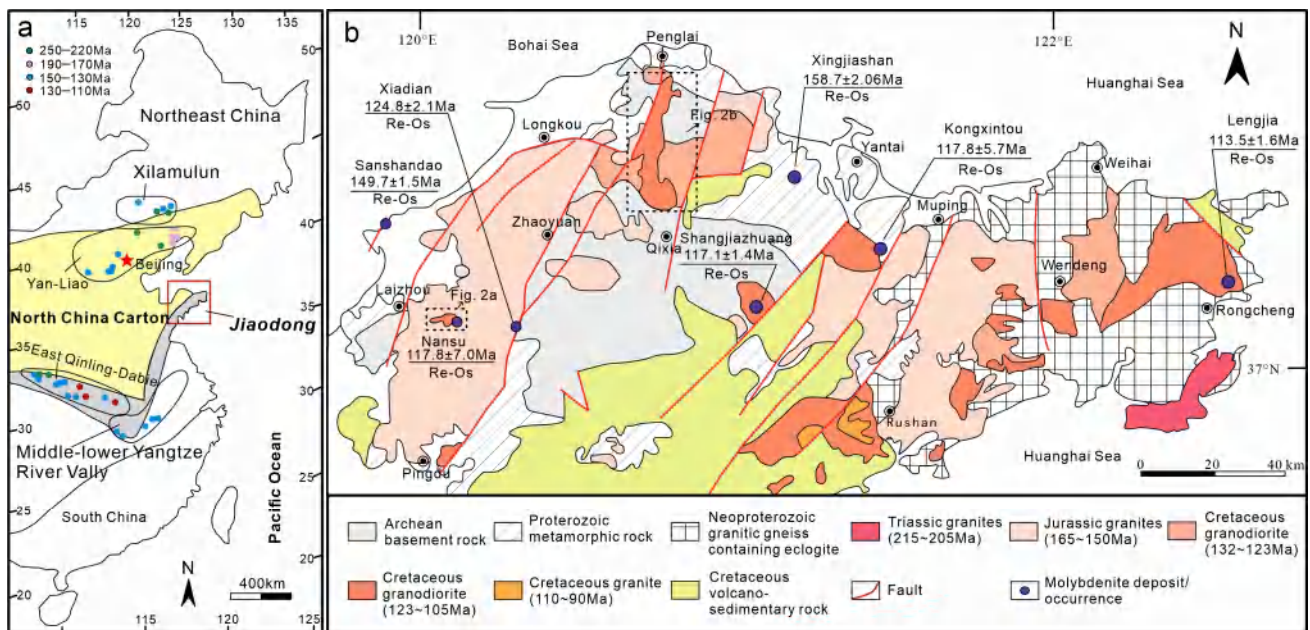
Figure 1. Spatial and temporal distribution of Mesozoic Mo-bearing deposits in eastern China (**a**) and simplified geological map of the Jiaodong area (**b**) (modified after [59]). Molybdenite Re-Os dating data are from [58,59,62–66].

2.2. Geology of Ore Deposits and Related Granitoids

2.2.1. Nansu Mo Occurrence

The Nansu pluton, located in the south of Laizhou City, belongs to the Late Early Cretaceous granitoid in Jiaodong. The pluton intrudes into the Late Jurassic granite in the form of stock, with a small scale, and its outcrops cover an area of about 15 km^2 (Figure 1). The Nansu pluton has a "dual core" girdle structure, with the lithology of two cores being granodiorite and the lithology of the marginal facies being monzogranite, and a small amount of quartz monzonite at the margin of the pluton (Figure 2a). Granodiorite in the core of Nansu pluton hosts a Mo occurrence, which is associated with molybdenite mineralization. The sampling coordinates are 120°06′53″ E, 37°09′01″ N.
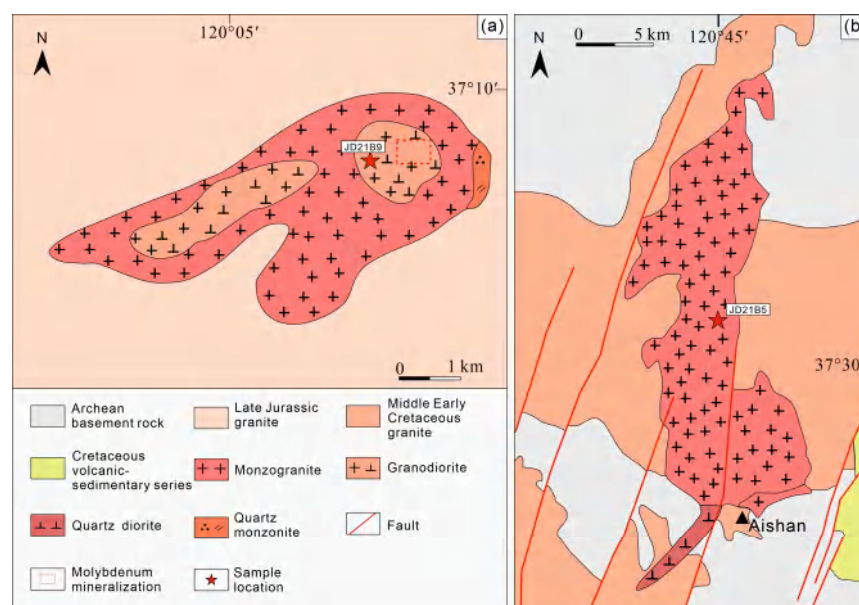
Figure 2. Geological map of Nansu pluton (**a**) and Aishan pluton (**b**) (modified after [67]).

The collected sample (21JDB9) is named fine-grained granodiorite with porphyritic texture and massive structure. Granodiorite is mainly composed of plagioclase (45%–50%), K-feldspar (20%–25%), quartz (10%–15%), biotite and hornblende (about 10%). It contains accessory minerals such as apatite, titanite, zircon, allanite, and a small amount of magnetite (Figure 3).
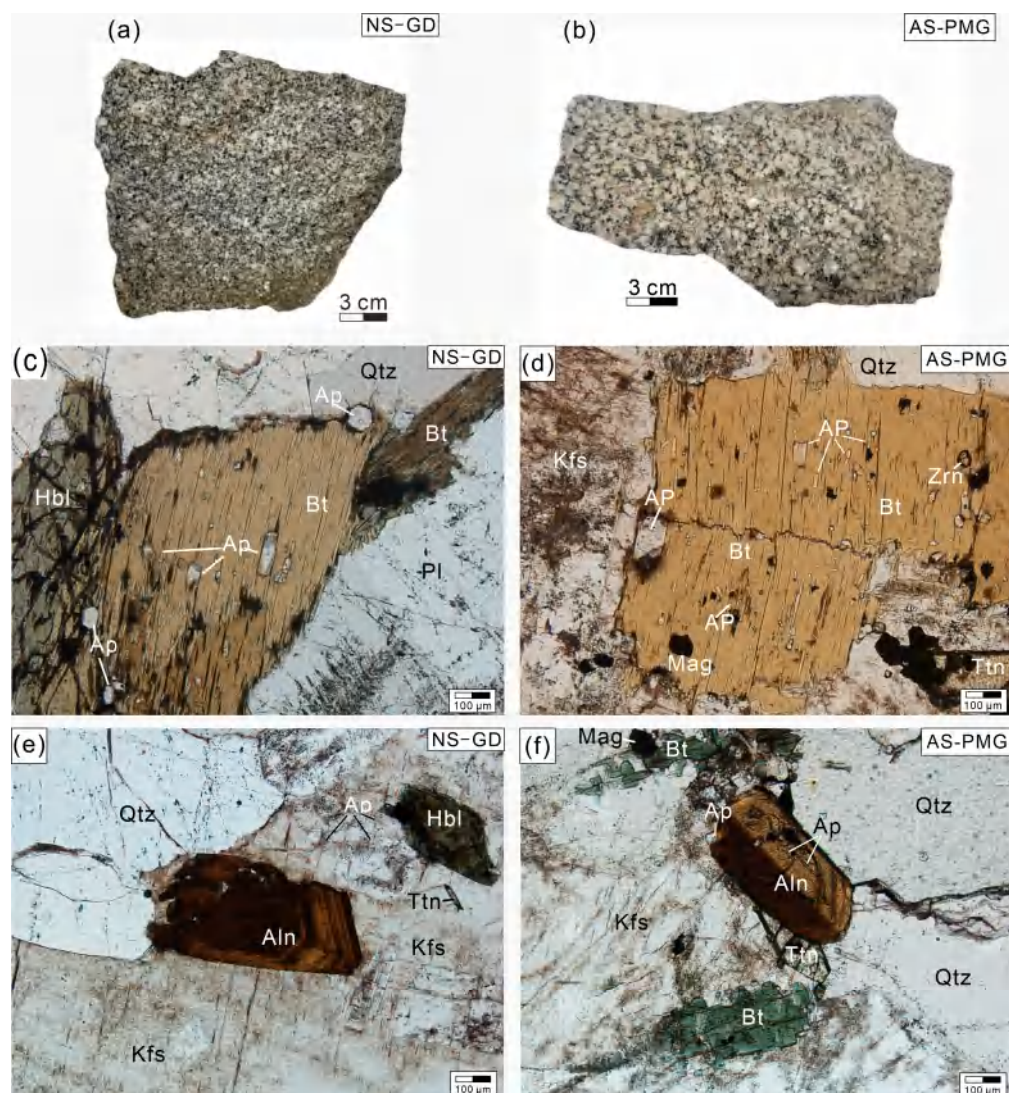
Figure 3. Petrographical characteristics of the Nansu and Aishan pluton. (**a**) A hand specimen of Nansu granodiorite (NS-GD). (**b**) A hand specimen of Aishan porphyritic monzogranite (AS-PMG). (**c**) Photomicrograph of mineral assemblages of apatite in Nansu granodiorite. (**d**) Photomicrograph of mineral assemblages of apatite in Aishan monzogranite. (**e**) Photomicrograph of apatite associated with minerals such as titanite and allanite in Nansu pluton. (**f**) Photomicrograph of apatite associated with minerals such as titanite and allanite in Aishan pluton. Ap—apatite; Qtz—quartz; Kfs—potassium feldspar; Pl—plagioclase; Hbl—hornblende; Bt—biotite; Mag—magnetite; Aln—allanite; Ttn—titanite; Zrn—zircon.

Molybdenite mineralization is extensively present in the Nansu granodiorite. Molybdenite is mostly disseminated or veinlet in the edge and interior of quartz veins in granite. It is occasionally distributed in granite in aggregate form, and a small amount is distributed along the lineation of tectonic scratches on the late tectonic joint surface of granite.

2.2.2. The Aishan Pluton

The Aishan pluton is located in the central north of the Jiaobei Terrane, between Qixia and Penglai, and intrudes into the Middle Early Cretaceous granite in the form of apophyse, with an exposed area of about 250 km^2 (Figure 1). This pluton consists of two lithologies, including the main body of monzogranite and a small amount of quartz diorite at the edge (Figure 2b). The Aishan pluton and wall rock are mainly in intrusive and fault contact, showing an obvious contact boundary between early basic gneiss and granite. Both the Aishan and Nansu pluton belong to the Late Early Cretaceous granite in Jiaodong, but no mineralization has been found in the Aishan pluton, which belongs to ore-barren granitoid.

The collected sample from the Aishan pluton is medium-grained porphyritic monzogranite (21JDB5, geographical coordinates of 120°45′31″ E, 37°30′54″ N). It is mainly composed of plagioclase (35%–40%), K-feldspar (25%–30%), quartz (15%–20%), biotite (5%) and hornblende (4%). Accessory minerals are dominated by apatite, zircon, allanite, and magnetite (Figure 3).

3. Characteristics of Apatite and Analysis Methods

3.1. Features of Apatite

Samples analyzed in this study were fresh granitoids from the Nansu pluton associated with molybdenum mineralization and the ore-barren Aishan pluton of the late Early Cretaceous in the Jiaodong Peninsula. Under the optical microscope, apatite grains in granitoids are mostly subhedral to euhedral, hexagonal columnar or long columnar. Many acicular apatites also developed within the Nansu granodiorite (NS-GD), which may be formed by rapid cooling of magma under the circumstance of magma mixing. Most apatite grains exist as inclusions in biotite, hornblende, K-feldspar, plagioclase, and quartz (Figure 3), indicating that the apatite crystallized in the early stages of magmatism and was not affected by late fractional crystallization. In addition, some apatites occur as groundmass intergranular apatites.

Apatite grains from the NS-GD are subhedral to euhedral, hexagonal, elongated and acicular (Figure 3c). Most apatite grains commonly occur as inclusions of biotite, hornblende, K-feldspar, and quartz. Additionally, minor apatite inclusions can be observed in minerals like allanite, titanite, and zircon (Figure 3e). They also grow on the edge of magnetite and coexist with magnetite. The size of apatite in the Nansu pluton is relatively variable, ranging from 30 to 500 μm.

Abundant subhedral to euhedral apatite grains occur in the Aishan monzogranite. They are mostly hexagonal columnar crystal forms, with a variable particle size ranging from 30 to 300 μm (Figure 3d). Apatite is mainly presented in biotite, quartz, and matrix, but apatite inclusions also occur in the grains of allanite, titanite, and zircon (Figure 3f).

3.2. Analytical Methods

The fresh granitoid samples of the two plutons were ground into probe pieces and observed under the optical microscope to find apatite and circle points. Then, the electron microprobe was used for quantitative analysis of major elements and in situ LA-ICP-MS trace elements analysis.

3.2.1. Major Element Analyses

Apatite major elements (wt. %) compositions were determined by electron microprobe analysis using a JEOL JXA-8230 electron microprobe at Shandong Institute of Geological Sciences, China. The voltage selected for this analysis is 15 kV acceleration voltage, electron beam current is 1×10^{-8} A, and beam spot diameter is 3 μm. The test components include CaO, P_2O_5, Na_2O, MgO, Al_2O_3, SiO_2, FeO, MnO, SO_3, TiO_2, Cr_2O_3, F, and Cl. Standards used were natural minerals and synthetic compounds, the specific mineral is apatite (Ca-P), Sr Lapis Lazuli (Sr), jadeite (Si, Na), almandine garnet (Al, Fe), diopside (Ca, Mg), sanidine (K), rutile (Ti), rhodonite (Mn), nickel (Ni), chromium oxide (Cr), tugtupite (Cl), and topaz (F). The data were corrected using the ZAF correction method of Japan Electronics (JEOL).

3.2.2. Trace Element Analyses

In situ analysis of trace elements in apatite microzone was conducted at the testing center of Shandong Bureau of China Metallurgical Geology Administration. GeoLasPro 193 nm ArF excimer system produced by Conherent (USA) and Thermo Fisher ICAP Q quadrupole ICP-MS were combined for the experiments. The laser denudation process uses helium (He) as a carrier gas, which carries sample aerosols through a T-connector and is mixed with argon (carrier gas, plasma gas, and compensating gas) before entering the ICP. The test system is optimized by adjusting the gas flow of helium and argon to obtain the best signal of NIST SRM 610 (the standard reference material for synthetic silicate glass developed by the National Institute of Standards and Technology). The optimum conditions are the highest signal sensitivity, the lowest oxidation yield, the lowest double charge interference, the lowest gas gap, and the most stable signal strength. The beam spot diameter is 40 μm, the frequency is 6 Hz, and the energy density is about 10–12 J/cm^2. The external calibration standards were NIST SRM 610, NIST SRM612, BCR-2G, and BIR-1G, and the monitoring samples were CGSG-1 and CGSG-2. The sampling methods were single-point denudation and peak hopping acquisition. We inserted a sub-sample NIST610, NIST612 and a monitored the sample every 5–10 sample points. The element content of the sample was calculated using the ICPMSDATACAL data processing program.

3.2.3. Neodymium Isotopes

In situ Nd isotope analysis of apatite was determined on a Neptune Plus MC-ICP-MS (Thermo Fisher Scientific, Bremen, Germany) in combination with a J-200 343 nm femtosecond laser ablation system (Applied Spectra, West Sacramento, CA, USA) housed at the Nanjing Hongchuang Geological Exploration Technology Service Co., LTD, Jiangsu, China. The JET sample and the X-ray grazing cone are used together with the protective electrode (GE), and all measurements are taken in low-resolution and static mode. At the time of measurement, 7 mL/min of nitrogen was added from the sample pool to improve the sensitivity, and a buffer smoothing device was used before the ICP to reduce the fluctuation effect caused by laser-ablation pulses. At the beginning of each analysis phase, the fs-LA-ICP-MS system was optimized using NIST 612 for maximum signal strength and low oxidation rates. The sample was ablated in line mode, the beam energy density was 1.5 J/cm^2, the laser spot size was 50 μm, the segment moving speed was 0.65 μm/s, the pulse frequency was 8 Hz, and the integration time of background signal acquisition before ablation was 15 s. Based on the $^{146}Nd/^{144}Nd$ value of 0.7219 and $^{147}Sm/^{149}Sm$ value of 1.0868, the instrumental mass deviation of Nd and Sm isotopes was corrected using the exponential law function [68]. The interference of ^{143}Sm to ^{143}Nd was corrected according to the measured signal intensity, mass bias coefficient, and natural isotope composition of ^{147}Sm.

4. Results

4.1. Apatite Major and Halogen Elements

According to the analytical results (Table 1), there is no significant difference in CaO and P$_2$O$_5$ contents between ore-fertile and ore-barren granitoids, with CaO contents ranging from 51.76 to 55.54 wt. % and P$_2$O$_5$ contents ranging from 41.07 to 44.47 wt. %. The contents of other major elements were low, and the contents of TiO$_2$, Cr$_2$O$_3$, MnO, Na$_2$O, and MgO were mostly <0.17 wt. %.

Table 1. The major element (wt. %) test results of apatite in Aishan and Nansu plutons in Jiaodong.

Pluton	Lithology	Sample No.	P_2O_5	SO_3	Cl	CaO	TiO_2	Cr_2O_3	MnO	FeO	F	Na_2O	MgO	Al_2O_3	SiO_2	Total	X_F	X_{Cl}	X_{OH}	X_F/X_{Cl}
		JD21B5(1)-15-1	42.97	0.16	0.10	53.98	bdl.	bdl.	0.14	0.21	1.56	0.08	0.03	bdl.	0.41	98.94	0.42	0.01	0.57	29.09
		JD21B5(1)-8-1	42.17	0.34	0.07	54.36	0.03	bdl.	0.06	0.29	1.75	0.16	bdl.	bdl.	0.31	98.77	0.47	0.01	0.52	50.18
		JD21B5(1)-8-2	42.33	0.15	0.14	54.27	0.04	bdl.	0.07	0.12	2.19	0.16	0.02	bdl.	0.37	98.90	0.59	0.02	0.39	28.72
		JD21B5(1)-8-3	42.61	0.18	0.12	53.89	bdl.	0.07	0.07	0.28	2.38	0.20	0.03	bdl.	0.38	99.18	0.64	0.02	0.34	36.73
		JD21B5(1)-2-1	42.63	0.24	0.04	54.38	0.03	bdl.	0.07	0.17	1.97	0.16	0.04	0.02	0.23	99.14	0.53	0.01	0.47	94.15
		JD21B5(1)-5-1	43.24	0.05	0.04	54.68	bdl.	0.02	0.05	0.18	2.16	0.01	0.02	bdl.	0.31	99.85	0.57	0.01	0.42	100.66
		JD21B5(1)-5-2	42.55	0.13	0.05	54.54	0.02	bdl.	0.08	0.21	2.16	0.13	0.02	bdl.3	0.44	99.40	0.58	0.01	0.42	85.55
		JD21B5(1)-6-1	43.39	0.19	0.09	54.11	bdl.	bdl.	0.08	0.10	1.05	0.10	0.02	0.01	0.44	99.10	0.28	0.01	0.71	22.41
		JD21B5(1)-6-2	42.19	0.11	0.09	51.76	0.04	0.10	0.13	0.86	2.15	0.09	0.69	0.27	3.64	101.20	0.56	0.01	0.43	42.71
		JD21B5(1)-6-3	43.14	0.47	0.06	54.54	bdl.	0.02	0.07	0.19	3.30	0.32	0.01	bdl.	0.39	101.10	0.86	0.01	0.13	99.22
		JD21B5(1)-7-1	43.06	0.55	0.07	55.02	bdl.	0.01	0.03	0.12	2.00	0.14	bdl.	bdl.	0.34	100.48	0.53	0.01	0.46	54.99
		JD21B5(1)-7-2	43.72	0.08	0.10	54.78	bdl.	bdl.	0.05	0.07	1.90	0.07	0.02	bdl.	0.16	100.14	0.50	0.01	0.48	34.12
		JD21B5(1)-7-3	42.91	0.12	0.03	55.02	0.03	bdl.	0.08	0.08	0.91	0.18	bdl.	0.01	0.14	99.13	0.25	0.00	0.75	55.01
		JD21B5(1)-7-4	44.29	0.19	0.10	54.87	0.04	0.05	0.10	0.14	1.70	0.05	0.03	0.02	0.19	101.03	0.45	0.01	0.54	30.46
		JD21B5(1)-7-1(JIA)	43.53	0.08	0.05	55.54	0.06	0.03	0.04	0.22	3.09	0.01	0.01	bdl.	0.10	101.45	0.81	0.01	0.18	108.74
		JD21B5(1)-7-2(JIA)	43.07	0.15	0.07	55.25	0.05	bdl.	0.11	0.12	0.95	0.02	bdl.	bdl.	0.24	99.60	0.25	0.01	0.74	26.34
Aishan pluton	Medium grained porphyritic monzogranite	JD21B5(1)-7-3(JIA)	44.32	0.09	0.05	55.10	bdl.	bdl.	0.01	0.20	2.71	0.04	bdl.	0.02	0.19	101.58	0.71	0.01	0.29	101.28
		JD21B5(1)-7-4(JIA)	43.94	0.10	0.07	55.31	0.02	0.04	0.09	0.18	1.54	0.04	0.04	bdl.	0.33	101.02	0.40	0.01	0.58	38.73
		JD21B5(1)-7-5(JIA)	43.58	0.35	0.11	54.35	bdl.	bdl.	0.10	0.15	2.02	0.19	0.01	bdl.	0.36	100.34	0.53	0.02	0.45	35.56
		JD21B5(1)-7-6(JIA)	43.08	0.76	0.06	54.45	bdl.	bdl.	0.08	0.15	2.40	0.27	0.02	bdl.	0.53	100.79	0.63	0.01	0.36	74.76
		JD21B5(1)-7-7(JIA)	43.40	0.64	0.09	53.81	bdl.	0.01	bdl.	0.02	2.06	0.21	bdl.	0.01	1.19	100.54	0.54	0.01	0.45	44.61
		JD21B5(1)-7-8(JIA)	42.15	0.85	0.06	54.99	bdl.	0.01	0.06	0.13	2.47	0.32	bdl.	0.05	0.76	100.77	0.65	0.01	0.34	82.29
		JD21B5(1)-7-9(JIA)	42.60	0.28	0.05	54.98	bdl.	bdl.	0.02	0.17	0.95	0.09	0.02	bdl.	0.38	99.12	0.26	0.01	0.74	36.81
		JD21B5(1)-7-10(JIA)	43.27	0.11	0.07	54.59	bdl.	bdl.	0.03	0.27	1.36	0.05	0.01	bdl.	0.34	99.51	0.36	0.01	0.63	34.68
		JD21B5(1)-7-11(JIA)	44.36	0.10	0.08	55.30	bdl.	0.02	0.09	0.22	1.00	0.05	bdl.	0.03	0.23	101.03	0.26	0.01	0.73	24.90
		JD21B5(1)-7-12(JIA)	43.96	0.22	0.05	53.98	bdl.	bdl.	0.07	0.28	1.91	bdl.	bdl.	0.02	0.14	101.03	0.50	0.01	0.49	79.23
		JD21B5(1)-7-13(JIA)	44.02	0.15	0.04	55.21	0.03	bdl.	0.05	0.43	2.38	bdl.	bdl.	bdl.	0.10	101.51	0.62	0.01	0.37	103.10
		JD21B5(1)-7-14(JIA)	43.53	0.06	0.03	55.33	bdl.	0.01	0.07	0.43	2.95	bdl.	0.03	0.02	0.08	101.06	0.78	0.00	0.22	204.13
		JD21B5(2)-4-1	43.43	0.11	0.04	55.11	bdl.	bdl.	0.08	0.20	2.37	0.07	0.01	bdl.	0.29	99.51	0.63	0.01	0.36	100.46
		JD21B5(2)3-1	43.64	0.12	0.08	53.92	0.04	bdl.	0.11	0.11	1.66	0.14	0.03	bdl.	0.19	99.71	0.44	0.01	0.55	38.28
		JD21B5(2)5-1	43.78	0.17	0.09	54.32	bdl.	bdl.	0.08	0.17	2.52	0.04	0.01	0.01	0.33	100.76	0.66	0.01	0.33	49.98
		JD21B5(2)-10-1	42.82	0.16	0.06	54.65	0.03	bdl.	0.03	0.16	1.54	0.03	0.05	0.01	0.30	98.37	0.42	0.01	0.57	49.67
		JD21B5(2)-15-2	43.34	0.31	0.09	53.83	0.01	bdl.	0.14	0.01	1.68	0.21	bdl.	bdl.	0.21	99.83	0.45	0.01	0.54	36.01
		JD21B5(2)-12-1	41.91	0.22	0.17	54.55	0.02	bdl.	0.07	bdl.	1.95	0.13	bdl.	bdl.	0.38	97.42	0.53	0.02	0.44	22.08

Table 1. *Cont.*

Pluton	Lithology	Sample No.	P$_2$O$_5$	SO$_3$	Cl	CaO	TiO$_2$	Cr$_2$O$_3$	MnO	FeO	F	Na$_2$O	MgO	Al$_2$O$_3$	SiO$_2$	Total	X$_F$	X$_{Cl}$	X$_{OH}$	X$_F$/X$_{Cl}$
Nansu pluton	Fine-grained granodiorite	JD21B9(1)2-1	42.744	0.19	0.10	53.65	bdl.	bdl.	0.09	0.23	2.28	0.27	bdl.	0.02	0.51	99.10	0.61	0.01	0.37	43.03
		JD21B9(1)2-2	43.161	0.13	0.04	54.97	bdl.	bdl.	0.05	0.04	1.39	0.12	bdl.	bdl.	0.36	99.65	0.37	0.01	0.62	66.50
		JD21B9(1)-6-1	43.254	bdl.	0.10	54.17	bdl.	bdl.	0.02	0.07	1.47	0.19	0.01	bdl.	0.34	98.98	0.40	0.01	0.59	27.78
		JD21B9(1)-6-2	43.416	0.11	0.08	54.78	bdl.	bdl.	0.06	0.11	2.47	0.16	bdl.	0.02	0.51	100.66	0.65	0.01	0.34	59.18
		JD21B91-8-1	42.846	0.10	0.09	54.01	0.03	bdl.	0.14	0.25	1.38	0.56	0.01	bdl.	0.48	99.30	0.37	0.01	0.61	28.38
		JD21B91-8-2	41.92	0.40	0.09	52.73	bdl.	bdl.	0.12	0.26	2.47	0.22	bdl.	0.01	0.47	97.63	0.67	0.01	0.32	53.54
		JD21B9(2)-3-1	42.913	0.16	0.07	54.39	bdl.	bdl.	0.02	0.06	2.99	0.13	0.03	bdl.	0.35	99.83	0.79	0.01	0.20	84.47
		JD21B9(2)-3-2	42.649	0.11	0.09	54.39	bdl.	bdl.	0.13	0.30	1.98	0.33	0.05	bdl.	0.32	99.49	0.53	0.01	0.46	39.28
		JD21B9(2)-1-1	42.18	0.18	0.15	53.87	bdl.	0.03	0.07	0.22	2.37	0.52	0.01	0.02	0.64	99.22	0.63	0.02	0.34	29.03
		JD21B9(2)-7-2	42.364	0.11	0.06	52.97	bdl.	bdl.	0.01	0.07	2.20	0.08	bdl.	bdl.	0.46	97.38	0.60	0.01	0.39	65.12
		JD21B9(2)-6-1	44.004	0.18	0.03	53.58	bdl.	bdl.	0.10	0.10	2.67	0.14	bdl.	bdl.	0.28	99.94	0.70	0.00	0.29	171.72
		JD21B9(2)-6-2	43.247	0.14	0.07	54.15	bdl.	bdl.	0.07	0.26	3.15	0.10	bdl.	0.02	0.60	100.46	0.83	0.01	0.16	86.40
		JD21B9(2)-6-3	41.956	0.28	0.03	53.48	0.01	bdl.	0.07	0.17	2.49	0.09	bdl.	bdl.	0.54	98.05	0.67	0.00	0.32	178.47
		JD21B9(2)--4-1	42.135	0.25	0.08	54.05	bdl.	bdl.	0.08	0.09	2.48	0.10	bdl.	bdl.	0.69	98.87	0.66	0.01	0.32	58.48
		JD21B9(2)--4-2	41.885	0.10	0.09	53.55	0.07	bdl.	0.08	0.29	2.96	0.08	0.01	0.01	0.69	98.55	0.80	0.01	0.19	63.37
		JD21B9(2)--4-3	42.246	0.04	0.03	54.74	bdl.	bdl.	0.05	0.35	3.00	bdl.	0.01	0.02	0.67	99.88	0.80	0.00	0.20	215.00
		JD21B9(2)-9-3	41.068	bdl.	0.08	53.95	bdl.	bdl.	0.09	0.18	1.85	0.05	0.02	bdl.	0.63	97.12	0.51	0.01	0.48	42.14
		JD21B9(3)-1-1	42.932	0.12	0.04	54.39	bdl.	bdl.	0.15	0.04	1.30	0.05	0.01	0.02	0.26	98.73	0.35	0.01	0.64	69.09
		JD21B9(3)-1-2	44.473	0.07	0.07	54.69	bdl.	bdl.	0.16	0.11	1.13	0.10	bdl.	0.04	0.24	100.58	0.30	0.01	0.69	30.17
		JD21B9(3)-1-3	43.263	0.10	0.09	54.51	0.08	0.04	0.08	0.09	3.24	0.16	0.01	bdl.	0.37	100.65	0.85	0.01	0.13	64.35
		JD21B9(3)-1-4	44.053	0.09	0.03	54.27	0.07	0.02	0.10	0.11	2.38	0.16	0.01	bdl.	0.23	100.51	0.63	0.00	0.37	138.65

The ore-fertile Nansu granitoid has high F contents (average of 2.27 wt. %), low Cl contents (average of 0.07 wt. %), and high F/Cl ratio (average of 41.20). However, the F/Cl ratio of the ore-barren Aishan granitoid (the average F content of 1.96 wt. %, the average Cl content of 0.073 wt. %, and the average F/Cl ratio of 32.41) is lower than that of the ore-fertile granitoid. As shown in Figure 4, in the ternary diagram of apatite F-Cl-OH, apatite grains from the Nansu and Aishan plutons all have high F content and belong to fluorapatite. A method proposed by Ketcham (2015) [69] to estimate the OH contents in apatite according to the anion content measured by EMPA is used to calculate the OH contents of these two plutons. Among them, the OH contents in the Nansu pluton range from 0.26 to 1.38, with an average value of 0.78, and the OH contents in the Aishan pluton range from 0.24 to 1.51 with an average value of 0.94.
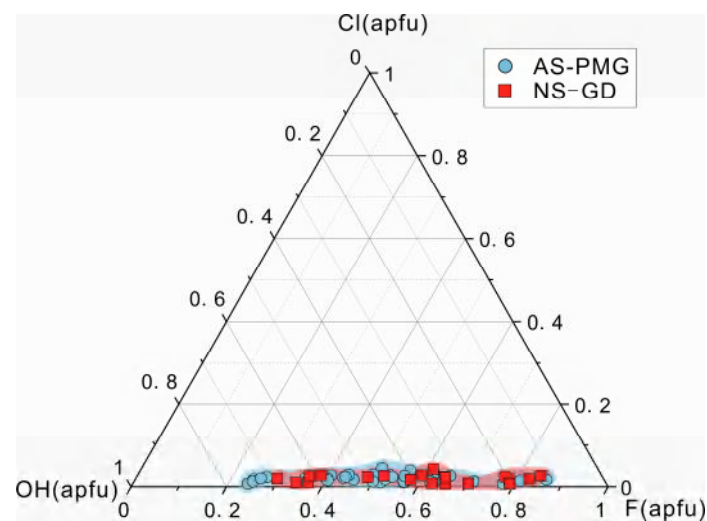

Figure 4. Ternary diagram of F, Cl, and OH in apatites from the Nansu pluton and Aishan pluton. Chlorine and F contents were determined by microprobe; OH was estimated by calculation of stoichiometry following a new method proposed by [69]. AS-PMG: porphyritic medium-grained monzonitic granite of the ore-barren granitoid Aishan pluton; NS-GD: fine-grained granodiorite of the ore-fertile granitoid Nansu pluton.

The SO_3 content of the ore-barren Aishan granitoid is 0.05–0.85 wt. %, with an average value of 0.24 wt. %, while the SO_3 content of the ore-fertile Nansu granitoid (with an average value of 0.14 wt. %) is relatively low (Table 1).

4.2. Apatite Trace Elements

The obtained results of trace elements in apatite are shown in Table 2. As can be seen from Figure 5, the apatite grains from the ore-fertile and ore-barren granitoid plutons are enriched in rare earth elements (REEs), and the chondrite-normalized REE patterns of the apatites are all above the whole rock. All the apatite grains have a "right-leaning" chondrite–normalized rare earth element (REE) pattern, with relative enrichment in light REEs and depletion in heavy REEs. Both the Nansu and Aishan plutons display moderately negative Eu anomalies (averages of δEu values are 0.44 and 0.51, respectively) and slightly positive Ce anomalies (averages of δCe values are 1.08 and 1.11, respectively). The Nansu pluton has the highest total REE contents, ranging from 5856 to 15,032 ppm, with an average of 10,750 ppm, while the total rare earth content in the Aishan pluton ranges from 3610 to 8007 ppm, with an average of 5280 ppm.

Table 2. The trace element (ppm) analytical results of apatite in Aishan and Nansu pluton in Jiaodong.

Pluton	Lithology	Sample No.	Sc	V	Cr	Co	Ni	Cu	Zn	Ga	Ge	As	Se	Rb	Sr	Y	Zr	Nb	Mo	Pd	Cd
Aishan pluton	Medium-grained porphyritic monzogranite	JD21B5-1-7-1	0.41	8.04	bdl.	0.05	0.30	0.03	0.69	7.31	8.53	7.19	9.78	bdl.	168.10	376.32	0.26	0.01	bdl.	0.34	0.08
		JD21B5-1-7-2	0.24	20.31	0.83	0.13	0.59	0.53	0.23	7.06	10.07	7.58	8.72	0.04	185.41	387.25	1.52	0.01	bdl.	0.51	0.13
		JD21B5-1-7-3	0.27	8.02	0.21	bdl.	bdl.	0.27	bdl.	5.34	6.87	10.42	7.86	0.11	334.39	359.59	0.43	0.03	0.17	0.60	0.11
		JD21B5-1-7-4	0.37	6.41	bdl.	0.09	bdl.	bdl.	bdl.	6.24	9.92	6.74	10.76	0.01	186.85	385.25	0.24	0.01	0.08	0.47	0.21
		JD21B5-1-8-1	0.42	38.05	2.19	4.87	8.54	6.05	69.11	12.87	10.02	6.32	8.36	60.22	220.07	302.84	1.56	2.15	bdl.	0.43	0.25
		JD21B5-2-3	0.27	23.18	0.27	0.10	1.08	0.17	0.90	6.77	7.14	4.96	9.65	bdl.	285.53	261.62	1.95	bdl.	0.07	0.26	0.08
		JD21B5-2-5-1	0.43	12.04	bdl.	bdl.	bdl.	bdl.	bdl.	6.20	8.69	6.85	7.42	0.02	224.25	405.48	0.66	0.06	bdl.	0.64	0.13
Aishan pluton	Medium-grained porphyritic monzogranite	JD21B5-2-10	0.25	15.82	0.95	0.04	0.19	0.14	bdl.	8.13	10.75	5.77	13.36	0.03	207.84	401.15	1.45	0.02	bdl.	0.42	0.20
		JD21B5-2-12	0.50	10.84	0.08	0.11	0.84	0.29	bdl.	11.71	14.52	5.83	11.55	0.03	205.72	476.83	1.08	0.01	0.52	0.48	bdl.
Nansu pluton	Fine-grained granodiorite	JD21B9-1-2	0.36	24.98	bdl.	0.13	bdl.	0.11	0.41	15.43	18.31	11.23	18.45	bdl.	257.44	693.25	5.36	0.05	bdl.	1.29	bdl.
		JD21B9-1-6-1	0.22	7.49	0.42	0.11	1.21	0.58	bdl.	12.65	14.84	7.51	18.40	0.17	493.15	451.63	0.59	0.05	0.03	0.59	bdl.
		JD21B9-1-6-2	0.26	19.21	0.23	0.19	1.05	3.03	0.45	18.08	22.82	11.75	17.14	0.10	291.15	785.75	1.88	0.06	0.06	0.95	bdl.
		JD21B9-1-8-1	0.10	37.17	0.90	0.09	bdl.	0.18	1.18	9.54	11.56	3.93	9.69	0.01	264.12	418.89	3.61	bdl.	bdl.	0.51	bdl.
		JD21B9-1-8-2	0.32	11.72	1.13	0.04	0.87	bdl.	0.38	20.88	24.33	12.25	17.39	bdl.	327.76	608.19	2.30	0.01	0.07	0.72	bdl.
		JD21B9-2-1-1	0.56	12.69	0.31	0.05	0.17	0.06	bdl.	17.05	20.32	9.34	14.82	0.14	258.27	758.90	1.56	0.05	0.03	0.58	bdl.
		JD21B9-2-3-1	0.46	11.78	0.73	0.05	0.60	0.13	1.09	17.48	20.20	9.98	19.09	0.10	507.44	565.51	1.20	0.04	0.07	0.72	bdl.
		JD21B9-2-3-2	0.01	29.92	0.10	0.19	0.84	1.20	1.94	7.65	8.14	4.68	7.85	0.45	387.86	287.72	0.27	0.03	0.08	0.31	bdl.
		JD21B9-2-4	0.64	10.67	bdl.	0.09	bdl.	bdl.	0.91	19.26	25.58	13.22	27.10	0.11	305.28	746.98	4.08	0.02	0.15	0.43	0.60
		JD21B9-3-1-1	0.54	12.39	0.99	0.11	bdl.	bdl.	0.47	19.67	21.92	10.95	25.93	bdl.	420.30	608.35	3.17	0.03	bdl.	0.82	bdl.
		JD21B9-3-1-3	bdl.	7.15	0.63	bdl.	1.75	0.04	bdl.	10.32	11.58	6.94	7.09	0.07	347.50	453.17	0.57	bdl.	bdl.	0.87	0.10
		JD21B9-3-1-4	0.18	7.17	1.33	0.25	0.68	0.29	bdl.	8.79	9.15	6.01	12.46	0.09	495.61	323.08	0.53	0.03	bdl.	0.64	bdl.

Pluton	Lithology	Sample No.	Sn	Sb	Cs	Ba	La	Ce	Pr	Nd	Sm	Eu	Gd	Tb	Dy	Ho	Er	Tm	Tb	Lu	Hf
Aishan pluton	Medium-grained porphyritic monzogranite	JD21B5-1-7-1	0.23	0.09	bdl.	0.40	930.76	2289.78	267.32	1072.03	160.30	21.99	116.03	12.46	62.50	11.45	34.21	4.47	27.02	4.73	0.03
		JD21B5-1-7-2	0.29	bdl.	0.05	0.27	1011.25	2417.71	289.18	1190.70	176.61	22.66	122.69	13.14	65.79	12.14	35.19	4.48	27.33	4.56	0.04
		JD21B5-1-7-3	0.36	bdl.	0.01	0.08	531.66	1525.85	198.35	902.70	159.14	20.06	118.71	13.09	63.31	11.50	33.63	4.11	23.71	4.03	0.08
		JD21B5-1-7-4	0.21	0.01	bdl.	0.15	746.66	2018.10	256.18	1078.60	171.11	22.32	121.28	12.97	66.83	12.44	35.43	4.41	26.85	4.54	0.04
		JD21B5-1-8-1	0.32	0.01	3.41	29.28	1144.94	2518.95	287.05	1088.50	154.92	22.42	98.41	10.68	53.33	8.99	25.46	3.53	21.28	3.37	0.15
		JD21B5-2-3	0.12	0.01	0.02	0.55	981.08	2328.47	264.49	1025.36	139.18	19.70	90.77	9.86	44.66	8.56	24.34	2.95	17.36	2.78	0.02
		JD21B5-2-5-1	0.18	0.02	bdl.	0.07	605.84	1881.22	246.02	1062.27	161.86	23.07	119.47	12.42	65.67	12.22	36.10	4.80	29.76	5.01	0.12
		JD21B5-2-10	0.11	0.02	bdl.	0.49	1102.72	2818.87	354.43	1440.26	201.79	29.13	133.06	14.48	71.82	12.58	36.60	4.87	28.07	4.26	0.05
		JD21B5-2-12	0.38	bdl.	0.01	0.58	1525.78	3665.32	441.06	1740.79	242.40	33.60	155.59	16.65	84.63	15.34	42.39	5.37	32.63	5.17	0.04

Table 2. *Cont.*

Pluton	Lithology	Sample No.	Sn	Sb	Cs	Ba	La	Ce	Pr	Nd	Sm	Eu	Gd	Tb	Dy	Ho	Er	Tm	Tb	Lu	Hf
Nansu pluton	Fine-grained granodiorite	JD21B9-1-2	0.21	0.09	0.02	0.38	2119.72	5000.25	602.78	2338.74	336.03	31.50	222.59	24.32	113.52	20.97	59.54	7.77	51.34	8.29	0.08
		JD21B9-1-6-1	0.19	0.01	bdl.	0.30	1921.12	4354.36	500.15	1904.47	265.71	31.60	169.18	17.88	82.65	14.24	38.72	4.84	26.29	4.07	0.06
		JD21B9-1-6-2	0.19	bdl.	bdl.	0.04	2636.59	6233.42	719.34	2662.32	366.34	39.82	230.17	25.50	123.89	22.89	66.87	8.86	57.95	9.36	0.06
		JD21B9-1-8-1	0.11	bdl.	0.01	0.30	1411.11	3305.40	369.77	1357.61	178.96	18.67	116.24	12.46	63.51	11.06	32.41	4.76	29.66	5.14	0.03
		JD21B9-1-8-2	0.18	0.04	0.01	0.44	3364.16	7277.33	780.24	2762.88	338.03	40.51	211.90	22.60	107.62	18.27	51.14	7.11	43.08	7.06	0.05
		JD21B9-2-1-1	0.12	bdl.	0.03	0.24	2495.06	5947.68	668.52	2494.22	338.81	37.31	219.61	23.81	115.87	21.00	62.91	8.67	54.55	9.27	0.06
		JD21B9-2-3-1	0.19	0.01	bdl.	0.70	2992.99	6429.00	677.56	2393.94	300.68	36.52	184.16	20.12	95.32	16.67	47.45	6.43	37.31	5.83	0.02
		JD21B9-2-3-2	0.21	0.05	0.17	0.33	1251.92	2830.96	300.29	1107.24	142.76	15.56	92.47	9.86	46.54	8.45	23.75	3.20	19.92	3.32	0.03
		JD21B9-2-4	0.21	bdl.	bdl.	0.27	3165.80	7003.93	788.69	2907.08	366.21	43.31	229.87	25.97	121.70	21.18	63.41	8.39	56.51	8.78	0.03
		JD21B9-3-1-1	0.40	0.08	0.03	0.16	3344.23	7040.13	747.24	2718.43	340.61	42.26	213.18	22.29	106.99	18.52	50.85	6.77	41.45	6.14	0.07
		JD21B9-3-1-2	0.01	bdl.	0.01	0.76	1817.23	4004.59	434.97	1634.80	212.45	26.24	132.79	14.45	68.65	12.18	33.35	4.39	25.99	3.89	0.05
		JD21B9-3-1-3	bdl.	bdl.	bdl.	0.31	1606.61	3819.55	425.90	1603.90	216.60	24.59	134.90	14.93	72.88	12.93	37.27	5.01	32.22	5.12	0.02
		JD21B9-3-1-4	0.06	0.01	bdl.	0.91	1516.02	3272.70	341.96	1247.76	156.33	20.35	101.74	10.79	51.87	9.19	26.67	3.55	20.32	3.18	0.03

| Pluton	Lithology	Sample No.	Ta	W	Bi	Pb	Th	U	ΣREE	δEu	δCe	(Sm/Yb)N	(La/Sm)N	(La/Yb)N	Sr/Y	Ce/Pb	Th/U	Ba/Th	Sr/Th	U/Th	La/Sm
Aishan pluton	Medium-grained porphyritic monzogranite	JD21B5-1-7-1	bdl.	0.02	0.58	5.35	36.29	49.77	5015.04	0.49	1.11	6.59	3.75	24.71	0.45	428.28	0.73	0.01	4.63	1.37	5.81
		JD21B5-1-7-2	bdl.	0.86	0.51	5.42	42.89	42.07	5393.438	0.47	1.08	7.18	3.70	26.54	0.48	446.40	1.02	0.01	4.32	0.98	5.73
		JD21B5-1-7-3	bdl.	4.44	1.37	4.60	28.94	33.86	3609.845	0.45	1.15	7.46	2.16	16.09	0.93	332.02	0.85	0.00	11.55	1.17	3.34
		JD21B5-1-7-4	0.01	0.12	0.50	4.53	22.73	46.80	4577.715	0.47	1.13	7.08	2.82	19.95	0.48	445.75	0.49	0.01	8.22	2.06	4.36
		JD21B5-1-8-1	0.06	0.33	0.55	10.53	40.31	42.25	5441.847	0.56	1.05	8.09	4.77	38.59	0.73	239.27	0.95	0.73	5.46	1.05	7.39
		JD21B5-2-3	0.01	bdl.	0.12	5.06	18.49	5.25	4959.563	0.54	1.10	8.91	4.55	40.53	1.09	460.44	3.52	0.03	15.45	0.28	7.05
		JD21B5-2-5-1	bdl.	2.17	0.91	4.65	36.18	43.37	4265.73	0.51	1.19	6.04	2.42	14.60	0.55	404.81	0.83	0.00	6.20	1.20	3.74
		JD21B5-2-10	bdl.	0.19	0.47	5.29	44.77	17.03	6252.935	0.54	1.10	7.99	3.53	28.18	0.52	532.95	2.63	0.01	4.64	0.38	5.46
		JD21B5-2-12	0.02	0.26	0.45	5.71	78.74	16.99	8006.711	0.53	1.08	8.25	4.06	33.54	0.43	642.04	4.63	0.01	2.61	0.22	6.29
Nansu pluton	Fine- grained granodiorite	JD21B9-1-2	0.03	0.07	0.06	6.53	118.96	18.65	10,937.36	0.35	1.07	7.27	4.07	29.61	0.37	766.13	6.38	0.00	2.16	0.16	6.31
		JD21B9-1-6-1	0.01	0.57	0.17	5.50	94.66	15.28	9335.281	0.46	1.06	11.23	4.67	52.42	1.09	791.75	6.20	0.00	5.21	0.16	7.23
		JD21B9-1-6-2	0.02	0.58	0.37	5.48	139.43	26.32	13,203.32	0.42	1.09	7.02	4.65	32.64	0.37	1136.76	5.30	0.00	2.09	0.19	7.20
		JD21B9-1-8-1	bdl.	0.01	0.10	5.31	37.10	7.22	6916.756	0.40	1.10	6.70	5.09	34.12	0.63	622.35	5.14	0.01	7.12	0.19	7.89
		JD21B9-1-8-2	0.01	0.14	0.06	6.30	117.85	14.87	15,031.93	0.46	1.06	8.72	6.42	56.02	0.54	1155.31	7.92	0.00	2.78	0.13	9.95
		JD21B9-2-1-1	0.02	0.15	0.30	5.63	113.47	20.53	12,497.29	0.42	1.11	6.90	4.75	32.81	0.34	1055.85	5.53	0.00	2.28	0.18	7.36
		JD21B9-2-3-1	0.01	0.04	0.09	6.59	107.02	14.69	13,243.99	0.47	1.06	8.95	6.43	57.54	0.90	976.11	7.29	0.01	4.74	0.14	9.95
		JD21B9-2-3-2	bdl.	1.24	0.13	5.38	25.12	6.98	5856.251	0.41	1.10	7.96	5.66	45.07	1.35	526.04	3.60	0.01	15.44	0.28	8.77
		JD21B9-2-4	0.01	0.03	0.20	5.63	115.96	13.56	14,810.82	0.46	1.06	7.20	5.58	40.18	0.41	1244.21	8.55	0.00	2.63	0.12	8.64
		JD21B9-3-1-1	0.02	0.01	0.09	6.24	103.16	12.53	14,699.09	0.48	1.05	9.13	6.34	57.87	0.69	1128.66	8.23	0.00	4.07	0.12	9.82
		JD21B9-3-1-2	0.01	bdl.	0.10	5.96	90.11	13.09	8425.961	0.48	1.07	9.08	5.52	50.15	1.26	671.80	6.88	0.01	5.64	0.15	8.55
		JD21B9-3-1-3	bdl.	bdl.	0.12	5.44	86.90	12.18	8012.417	0.44	1.11	7.47	4.79	35.77	0.77	702.24	7.13	0.00	4.00	0.14	7.42
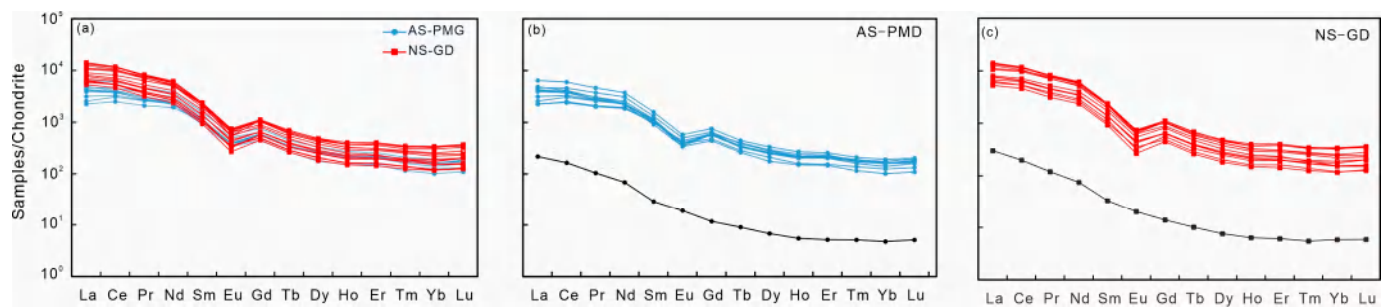
Figure 5. Chondrite-normalized rare earth element (REE) (**a**) patterns of apatite in granitoids from the Aishan pluton (**b**) and Nansu Pluton (**c**). The color line indicates the REE concentration of apatite, and the black line indicates the REE concentration of Whole rock. Whole rock REE data of the Aishan pluton and Nansu pluton are sourced from [70]. Chondrite and primitive mantle normalization values are from [71].

The contents of Sr and Y in apatite from ore-fertile and ore-barren granitoids are negatively correlated. The ore-fertile granitoids have relatively higher contents of Sr and Y. The contents of Sr in Nansu pluton vary from 257.44 to 508.29 ppm with an average value of 374.17 ppm, and the contents of Y vary from 287.72 to 785.75 ppm with an average value of 546.43 ppm. In contrast, the ore-barren Aishan pluton has Sr contents ranging between 168.10 and 334.39 ppm (average of 224.24 ppm), and Y contents ranging between 261.62 and 476.83 ppm (average of 372.93 ppm).

There are also some differences in Th, U, and Ce contents of apatite in ore-fertile and ore-barren granitoids (Table 2). The ore-fertile Nansu granitoid has the highest Th contents (25.12–139.43 ppm, average of 93.91 ppm), while the ore-barren Aishan granitoid has much lower Th contents of 18.49–78.74 ppm, with an average of 38.81 ppm. The U contents of Nansu pluton (6.98–26.32 ppm, average of 14.39 ppm) are relatively low, while the U contents of ore-barren granitoid Aishan pluton are the highest, ranging from 5.25 to 49.77 ppm (average of 33.04 ppm). The Ce contents of Nansu pluton range from 2830.96 to 7277.33 ppm, with an average of 5116.87 ppm, and those of Aishan pluton range from 1525.85 to 3665.32 ppm, with an average of 2384.92 ppm. These two plutons have no significant difference in Pb contents. The contents of Pb in Nansu pluton are 5.31–6.59 ppm, with an average value of 5.89 ppm, and the contents of Pb in Aishan pluton are 4.53–10.53 ppm, with an average value of 5.68 ppm.

4.3. In Situ Nd Isotope of Apatite

We selected six grains for in situ Nd isotopic determination and the results are presented in Table 3. The normalized $^{143}Nd/^{144}Nd$ ratios of the apatites in the Aishan pluton are varying between 0.51159 and 0.51164, and the normalized $^{143}Nd/^{144}Nd$ ratios of the apatites in the Nansu pluton are ranging between 0.51142 and 0.51157. The normalized $^{147}Sm/^{144}Nd$ ratios of the apatites in the Aishan pluton vary from 0.0937 to 0.0940, and the normalized $^{147}Sm/^{144}Nd$ ratios of the apatites in the Nansu pluton vary from 0.0887–0.0935. The $\varepsilon_{Nd}(t)$ values of the Nansu pluton were calculated at t = 115.7 Ma (zircon U-Pb age, date from [70]), ranging from −16.63 to −17.61, with an average value of −17.12. The $\varepsilon_{Nd}(t)$ values of the Aishan pluton were calculated at t = 116.8 Ma (zircon U-Pb age, date from [70]), ranging from −17.86 to −20.86, with an average of −19.31.

Table 3. Nd isotope data in Aishan and Nansu plutons in Jiaodong.

Pluton	Lithology	Sample No.	^{143}Nd/^{144}Nd	^{147}Sm(v)	^{146}Nd(v)	Ziron U-Pb Age (Ma)	$(^{147}$Sm/^{144}Nd)$_N$	$(^{143}$Nd/^{144}Nd)$_N$	ε_{Nd}(t)	T$_{DM1}$ (Ma)	T$_{DM2}$ (Ma)	Reference
Aishan pluton	Medium-grained porphyritic monzogranite	JD21B51-2-1	0.511658	0.69	0.087	115.7	0.0940	0.511587	−17.61	1897	2341	This paper
		JD21B51-2-2	0.511708	0.55	0.069	115.7	0.0937	0.511637	−16.63	1829	2262	
		JD21B52-4-1	0.511682	0.57	0.072	115.7	0.0940	0.511611	−17.13	1866	2303	
Nansu pluton	Fine-grained granodiorite	JD21B91-1-1	0.511644	0.76	0.095	116.8	0.0933	0.511572	−17.86	1904	2362	
		JD21B91-3-1	0.511575	0.49	0.062	116.8	0.0935	0.511504	−19.2	1993	2470	
		JD21B91-5-2	0.511486	0.5	0.06	116.8	0.0887	0.511419	−20.86	2025	2604	
Aishan pluton	Medium-grained porphyritic monzogranite	AS22-63-1	——	——	——	115.7	0.0734	0.511699	−16.49	——	2256	[70]
		AS22-65-1	——	——	——	115.7	0.0886	0.511702	−16.67	——	2269	
		AS22-65-2	——	——	——	115.7	0.0885	0.511708	−16.55	——	2260	
		AS22-64-1	——	——	——	115.7	0.0936	0.511713	−16.53	——	2257	
		AS22-64-2	——	——	——	115.7	0.0884	0.51171	−16.51	——	2256	
Nansu pluton	Fine-grained granodiorite	JD21B9	——	——	——	116.8	0.0879	0.511595	−18.73	——	2436	[70]
		JD21B10	——	——	——	116.8	0.0917	0.511472	−21.18	——	2635	
Aishan pluton	Granitoid	asb1	——	——	——	114	0.0814	0.511605	−18.5	——	——	[67]
		asb4	——	——	——	114	0.0727	0.511617	−18.1	——	——	
		asb5	——	——	——	118	0.0811	0.511587	−18.8	——	——	
Nansu pluton	Fine-grained granodiorite	nsb1	——	——	——	110.5	0.0705	0.511412	−22.1	——	——	
	Lamporphyre	JJHT-01	——	——	——	90	0.1287	0.512607	0.17	——	——	[72]
		JJHT-02	——	——	——	90	0.1185	0.512872	5.46	——	——	
		JJHT-04	——	——	——	90	0.1277	0.512603	0.11	——	——	
		JJHT-05	——	——	——	90	0.1274	0.51262	0.44	——	——	
		JJHT-06	——	——	——	90	0.1107	0.512616	0.56	——	——	
		JJHT-07	——	——	——	90	0.1128	0.512658	1.35	——	——	
		JJHT-08	——	——	——	90	0.1107	0.512615	0.54	——	——	
		JJHT-09	——	——	——	90	0.1255	0.512756	3.12	——	——	
	Diabase	09S71	——	——	——	90	0.1259	0.512707	2.16	——	——	[73]
	Hornblendophyre	09DZ38	——	——	——	166.6	0.0997	0.511190	12.88	——	2110.69	
	Diabase	09XC17	——	——	——	122.69	0.0919	0.511412	22.24	——	2894.27	
	Diabase	09XC18	——	——	——	126.3	0.1026	0.511547	19.9	——	2682.25	
	Gabbro	09J54	——	——	——	90	0.1287	0.512607	0.17	——	——	
	Gabbro	09J59	——	——	——	90	0.1185	0.512872	5.46	——	——	
	Gabbro	09J76	——	——	——	90	0.1277	0.512603	0.11	——	——	
	Diabase	09J86	——	——	——	90	0.1274	0.51262	0.44	——	——	
	Diabase	09J87	——	——	——	90	0.1107	0.512616	0.56	——	——	
	Spessartine	D-X-1	——	——	——	90	0.1128	0.512658	1.35	——	2110.69	[74]
	Camptonite	J435-3	——	——	——	90	0.1107	0.512615	0.54	——	2894.27	
	Spessartine	LI08-11	——	——	——	90	0.1255	0.512756	3.12	——	2682.25	[74]
	Spessartine	LI08-13	——	——	——	122.6	0.1040	0.511677	13.46	——	2477.81	
	Andesite porphyrite	LI08-14	——	——	——	124.6	0.0975	0.511642	17.95	——	2532.88	
	Spessartine	S186-4	——	——	——	204.1	0.0975	0.511763	15.61	——	2424.1	

Note: "——" represents no data.

5. Discussion

5.1. Comparison of Oxygen Fugacity and Water Content in Parental Magma of Ore-Fertile and Ore-Barren Granitoids

Ouyang Hegen (2023) [75] conducted a quantitative analysis of the oxygen fugacity and volatile contents of ore-forming magmas, revealing that ore-forming magmas associated with various types of porphyry-skarn Mo deposits across diverse tectonic environments are consistently characterized as oxidized and water-rich. By comparing the oxygen fugacities and water contents inferred from apatite compositions of the Nansu and Aishan pluton, the following discussion explores the controlling factors that underlie the metallogenic differences observed in the Late Aptian granitoids of Jiaodong.

5.1.1. Oxygen Fugacity

The content of Ce, Eu, and Ga in apatite serves as a valuable indicator for assessing the redox state of magma [20,28,76–78]. These elements exist in two ionic valence states as follows: Eu^{3+}/Eu^{2+}, Ce^{4+}/Ce^{3+}, and Ga^{3+}/Ga^{2+}. Since Eu^{3+}, Ce^{3+}, and Ga^{2+} possess ionic radii that are more akin to Ca^{2+}, they preferentially enter the apatite lattice, replacing Ca^{2+} [17,20,29,79]. Under oxidizing conditions, Eu, Ce, and Ga tend to exist in their higher valence states, leading to lower ratios of Eu^{2+}/Eu^{3+}, Ce^{3+}/Ce^{4+}, and Ga^{2+}/Ga^{3+} in the melt. Therefore, apatites crystallized from the oxidized magma exhibit higher Eu contents but lower Ce and Ga contents [28,78]. However, relying solely on the variation in the content of a single element in apatite to reflect the redox state of magma is inadequate, as changes in elemental contents can be influenced by various other factors. For example, the Eu anomaly observed in apatite is influenced not only by the oxidation state of the magma but also by the crystallization of plagioclase. While a single Eu anomaly or Ce anomaly alone cannot accurately reflect the redox state, the contrasting partitioning behaviors of Eu and Ce can be harnessed to determine the oxidation state of the parental magma [28,79].

In the δCe-δEu diagram of apatite (Figure 6a), the δEu value and δCe value of apatite grains from ore-fertile and ore-barren granitoids are negatively correlated, suggesting that the magma is formed in a relatively oxidizing environment. Both the Nansu and Aishan plutons show moderate Eu negative anomaly and slight Ce positive anomaly, indicating that the ore-fertile and ore-barren granitoids have relatively high oxygen fugacity. In the diagram of δEu-Ga of apatite (Figure 6b), the δEu of the Nansu pluton is similar to that of the Aishan pluton, and the Ga content of Nansu pluton is relatively high, which indicates that the apatite of Aishan pluton may be formed in a relatively oxidized environment. In addition, the $\log f(O_2)$ of the Nansu pluton is −13.8, and the $\log f(O_2)$ of the Aishan pluton is −13.6~−13.7 (Table 4), which is calculated by the content of major elements in hornblende of these two plutons [80]. Moreover, the calculated oxygen fugacity by the zircon trace element denotes that the $\log f(O_2)$ of the Nansu pluton is −14.8, and the Aishan pluton is −15.0 [70] (Table 4). The δCe, δEu, and Ga contents of apatite and the oxygen fugacity values calculated by hornblende and zircon all reflect that the oxygen fugacity values of the ore-fertile Nansu and ore-barren Aishan plutons are approximately equal. The parental magma of the Nansu and Aishan plutons is relatively oxidized. Therefore, oxygen fugacity is not the factor that controls the difference between the Late Aptian ore-fertile and ore-barren granitoids in the Jiaodong area.
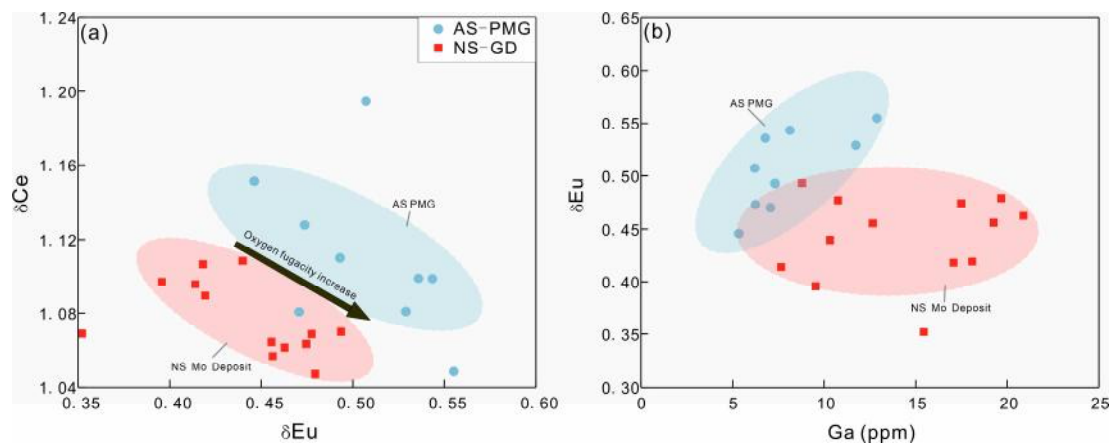
Figure 6. Binary diagram of δCe vs. δEu (**a**) and δEu vs. Ga (**b**) in apatite from the Aishan pluton and Nansu pluton. AS-PMG: porphyritic medium-grained monzonitic granite of the ore-barren granitoid Aishan pluton; NS-GD: fine-grained granodiorite of the ore-fertile granitoid Nansu pluton.

Table 4. Oxygen fugacity, volatile content and temperature and pressure data of magma in Aishan and Nansu pluton.

Pluton	Lithology	Sample No.	Mineral	log$f$ (O$_2$)	H$_2$O (wt.%)	F (wt.%)	Cl (wt.%)	P (MPa)	T (°C)	Reference
Nansu pluton	Porphyritic biotite monzogranite	LM-05/2B-1-2	Hornblende	−13.8	4.6	0.39	0.06	91.5	767	[70]
Aishan pluton	Porphyritic biotite hornblende granodiorite	WDS-05/1B-2-1		−13.6	4.9	0.5	0.02	104.7	777	
		WDS-05/1B-2-4		−13.7	5.0	0.43	0.03	105.7	776	
Nansu pluton	Fine-grained granodiorite	JD21B9	Zircon	−14.8	——	——	——	——	685	[81]
Aishan pluton	Medium-grained porphyritic monzogranite	JD21B5		−15.04	——	——	——	——	668	

Note: "— —" represents no data.

5.1.2. Water Content

Apatite is an important carrier of halogen elements, and apatite has strong corrosion resistance. Halogen elements entering apatite at high temperatures are generally not easily affected by later hydrothermal metasomatism. Many studies have used the concentration of OH in apatite to estimate the abundance of H$_2$O in the melt crystallized from apatite [19,23,82–88]. Studies have shown that the changes of F and OH in apatite are fairly consistent with the changes of F and H$_2$O in coexisting melt inclusions [22]. Therefore, it is a very effective way to estimate the water content in the coexisting melt by using the OH component in apatite. The results of apatite-melt partition experiments by McCubbin et al. (2015) [88] showed that the apatite-melt partition coefficient of OH is variable. Therefore, when using the apatite OH component to estimate the abundance of H$_2$O in the melt, it is necessary to combine the information of other components, such as the abundance of H$_2$O in apatite, the content of F and Cl in the melt, and the apatite-melt exchange distribution.

The OH contents of apatites from the Nansu and Aishan plutons are calculated by using the method proposed by Ketcham (2015) [69] to estimate the OH content according to the anion content in apatite determined by EMPA. The apatite OH contents of the Nansu pluton vary between 0.26 and 1.38, and those of the Aishan pluton range between 0.24 and 1.51. In the apatite F-Cl-OH ternary diagram (Figure 4), it can be noted that the OH distribution range of these two plutons is roughly the same.

The contents of major elements present in hornblende can provide valuable insights into estimating the water contents within the melt. According to our calculations, the melt H$_2$O content of the Nansu pluton stands at 4.6 wt. %. On the other hand, the H$_2$O contents of the Aishan pluton range from 4.9 to 5.0 wt. % (Table 4). Both of these plutons

exhibit relatively high magmatic water content. A comparison of the calculated water contents with the apatite OH contents indicates that both the ore-fertile and ore-barren granitoids share a similarly high magmatic water content. Therefore, it can be concluded that neither oxygen fugacity nor magmatic water content is responsible for the metallogenic differences observed between the Nansu and Aishan plutons. This result suggests that the ore-fertile granitoids possess a comparable crystalline environment to that of the ore-barren granitoids, thereby indicating that molybdenum mineralization is less associated with the crystalline environment and more probably occurs as a secondary or late-igneous event.

5.2. Distinctive Magmatic Evolution between Ore-Fertile and Ore-Barren Granitoids Revealed by Apatite

Because of the special structural characteristics of apatite, it can accommodate a variety of high concentrations of major and trace elements. It is a reliable indicator mineral for mineral exploration, which records and preserves the original information of magmatic and hydrothermal activities [11,20,28,29]. The variation of trace elements in apatite can be used to distinguish ore-fertile and ore-barren plutons and different deposit types [19,28,89]. Based on the machine learning method, Qiu et al. (2024) [89] used apatite trace element data to classify five different types of deposits and unmineralized apatites efficiently and accurately, indicating that apatite has the potential to distinguish mineralized and unmineralized plutons.

Sr is abundant in crustal rocks and can replace Ca^{2+} in apatite due to similar ionic radii during magmatic differentiation [90]. Early-crystallized apatite inherits Sr and Y compositional signatures of parental magma, making it a valuable indicator of magmatic source affinities. Prolonged magma storage in the deep crust is crucial for evolving water-bearing arc magmas, explosive volcanism, and economic magmatic-hydrothermal deposits [91]. A negative correlation between Sr and Y in apatite from the Nansu and Aishan plutons is observed in Figure 7a, with a variable Sr/Y ratio of 0.34–3.17. In Figure 7b, Sr is positively correlated with the Sr/Y ratio, and the Sr/Y ratio of the pluton decreases with magmatic differentiation. The Nansu granodiorite is characterized by higher apatite Sr content than the Aishan porphyritic monzogranite, indicating a relatively higher degree of magmatic fractionation in the ore-fertile system.
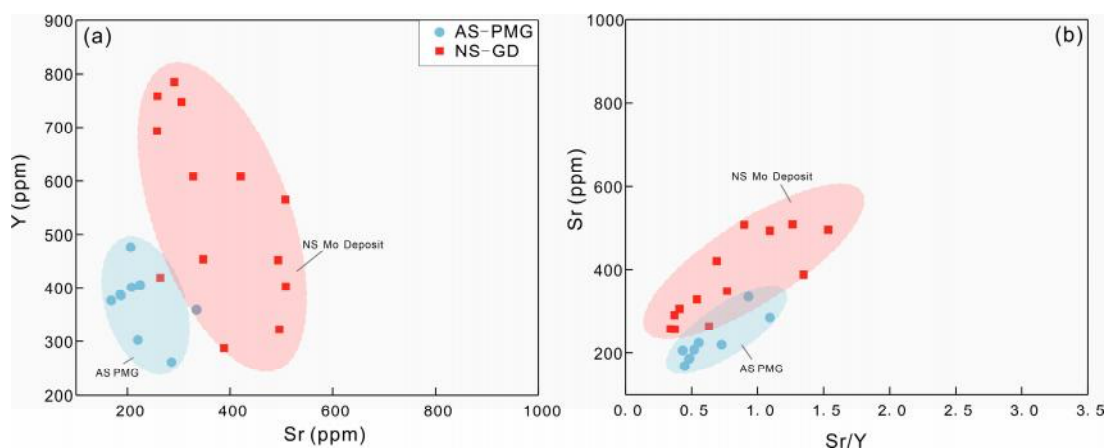
Figure 7. Binary diagram of Y vs. Sr (**a**) and Sr vs. Sr/Y (**b**) in apatite from the Aishan pluton and Nansu pluton. The symbols are the same as in Figure 6.

The concentration of trace elements in apatite is primarily influenced by several factors. Firstly, the geochemical composition of the magma source or parental magma has a significant influence. Secondly, the partitioning of trace elements between apatite and the silicate melt, as well as other minerals that have separated and crystallized either before or simultaneously with apatite, also contribute to its trace element content. Furthermore, recrystallization due to subsequent metamorphism can also affect the trace element concentration in apatite [20,21,91,92]. Experimental petrology studies have demonstrated that the partition co-

efficients of REEs between apatite and the melt can vary under different chemical and physical conditions. The MREEs exhibit a stronger affinity towards apatite compared to the LREEs and HREEs [9,65,86–88]. The whole-rock chondrite-normalized REE patterns of the Nansu and Aishan plutons display a right-leaning trend, with a slight Eu negative anomaly [61]. Since the apatites do not show a preference for LREEs and HREEs, the coherent right-leaning REE patterns in apatite grains and their host rocks imply a LREE-enriched source [89]. Changes in the trace element content of apatite may reflect variations in magma composition as minerals crystallize within the magma. The ratio of rare earth to other elements, such as $(Sm/Yb)_N$, $(La/Sm)_N$ and $(La/Yb)_N$, in apatite, combined with changes in Sr content, can be utilized to infer the crystallization process of the rock mass. As shown in Figure 8, a positive correlation can be observed between the $(Sm/Yb)_N$, $(La/Sm)_N$ and $(La/Yb)_N$ ratios and the Sr content of the Aishan and Nansu plutons. However, the decreasing trend in the $(Sm/Yb)_N$, $(La/Sm)_N$, and $(La/Yb)_N$ ratios within apatite suggests that the control of REE in apatite may be influenced by additional factors. One potential explanation for this decrease is the fractional crystallization of LREE-rich minerals, such as allanite and monazite, within the magma. This fractional crystallization can lead to a rapid decline in the ratios of $(Sm/Yb)_N$, $(La/Sm)_N$, and $(La/Yb)_N$ within apatite [79]. Our microscopic observations of the samples reveal the presence of allanite in both the Nansu and Aishan plutons (Figure 3), along with apatite inclusions within allanite particles. This observation provides a plausible explanation for the observed decrease in the $(Sm/Yb)_N$, $(La/Sm)_N$, and $(La/Yb)_N$ ratios during the magma separation process within the two plutons.
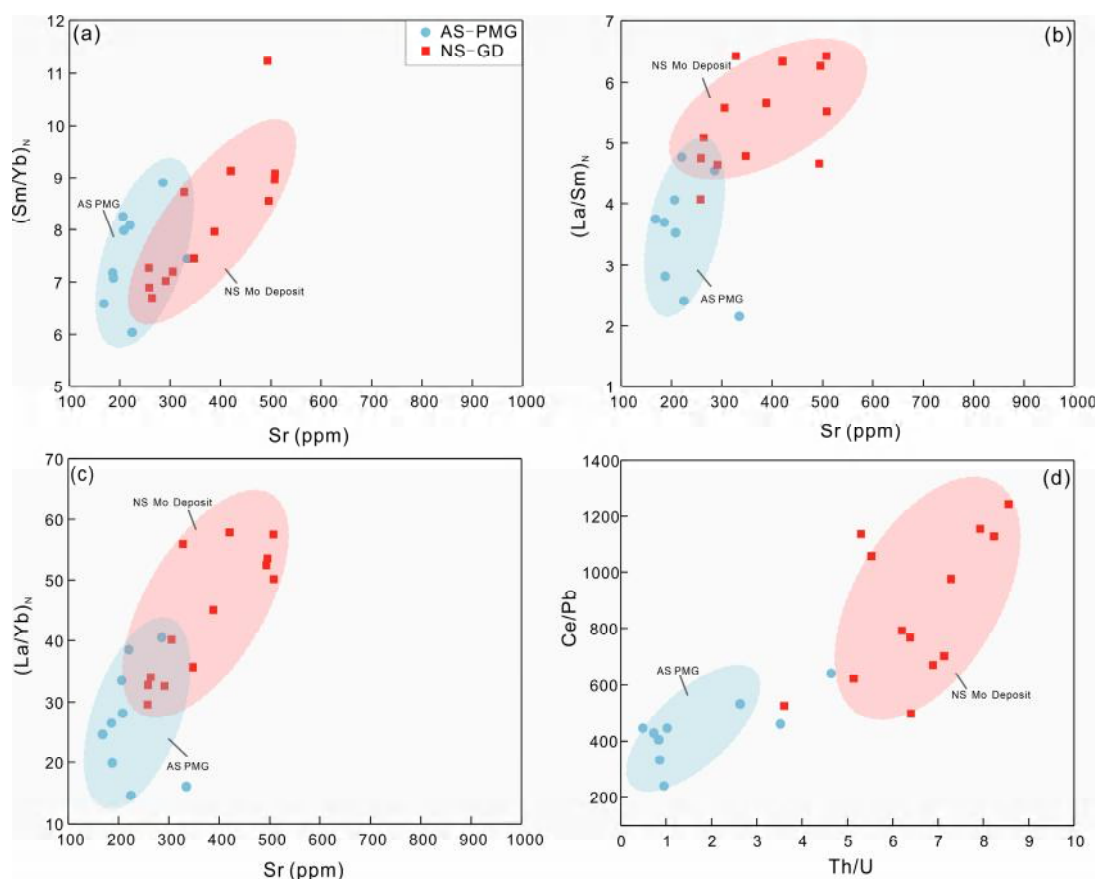
Figure 8. Binary diagram of $(Sm/Yb)_N$ vs. Sr (**a**), $(La/Sm)_N$ vs. Sr (**b**), $(La/Yb)_N$ vs. Sr (**c**) and Ce/Pb vs. Th/U (**d**) in apatite from the Aishan pluton and Nansu pluton. The symbols are the same as in Figure 6.

The activities of Pb, Ce, Th, and U in the subduction zone are different, which are 85%, 51%, 38%, and 29% [93], respectively. The activity of Pb, Ce, Th, and U in the subduction zone is the result of dehydration experiments on natural amphibolite in the upper mantle

under P/T conditions to study the subducted of trace elements in the dewatering process of subducting oceanic lithosphere [93]. At the same time, the incompatibility in the oceanic island basalt is Th > U ≈ Nb = Ta ≈ K > La > Ce ≈ Pb [71]. The order of trace element incompatibility in oceanic basalts was obtained using trace element data from MORBs and OIB [71]. The higher the Ce/Pb ratio, the lower the Th/U ratio, indicating stronger fluid activity. Compared with the ore-fertile granitoid, the Th/U value of the ore-barren granitoid varies in a small range, and the Ce/Pb value is also relatively low (Figure 8d). The average value of the Th/U ratio of apatite in ore-barren Aishan pluton is 1.74, and the average value of the Ce/Pb ratio is 436.88. The average value of the Th/U ratio of apatite in ore-fertile Nansu pluton is 6.50, and the average value of the Ce/Pb ratio is 867.30. The higher Ce/Pb ratio and relatively lower Th/U ratio of apatite from the ore-fertile Nansu pluton reflect that the magma at Nansu has more intensive fluid activity and a higher degree of magmatic differentiation during its formation. This is consistent with the view that the intensity of fluid activities in a magmatic system plays an important influence on the Mo potential of granitoids [75].

5.3. Differences in Magma Source between Ore-Fertile and Ore-Barren Granitoids

5.3.1. Apatite Nd Isotope as a Tracer of Magma Source

The Nd isotopic composition of apatite can effectively trace the source of magma [13,78,94–97]. The apatite $\varepsilon_{Nd}(t)$ value of the Nansu pluton is −17.86~−20.86, with an average of −19.31. The apatite $\varepsilon_{Nd}(t)$ values of Aishan pluton range from −16.63 to −17.61, with an average value of −17.12, which is consistent with the whole-rock $\varepsilon_{Nd}(t)$ value (Nansu pluton of −18.73, Aishan pluton of −16.55 [70]). The $\varepsilon_{Nd}(t)$-T diagram (Figure 9) shows that most of the whole-rock and apatite $\varepsilon_{Nd}(t)$ values of the Aishan pluton fall in the region of Proterozoic crust, and their corresponding T_{DM2} (depleted mantle model ages) are ranging from 2341 to 2262 Ma, with an average of 2302 Ma. The $\varepsilon_{Nd}(t)$ values of the Nansu pluton mainly fall into the region of the Archean crust, and their corresponding T_{DM2} ages vary between 2604 and 2362 Ma, with an average of 2479 Ma. From the Nd isotopic composition of apatite, the magma sources of the Nansu ore-fertile and Aishan ore-barren granitoids were mainly derived from the partial melting of the Precambrian metamorphic basement rocks (i.e., the Jiaodong group).
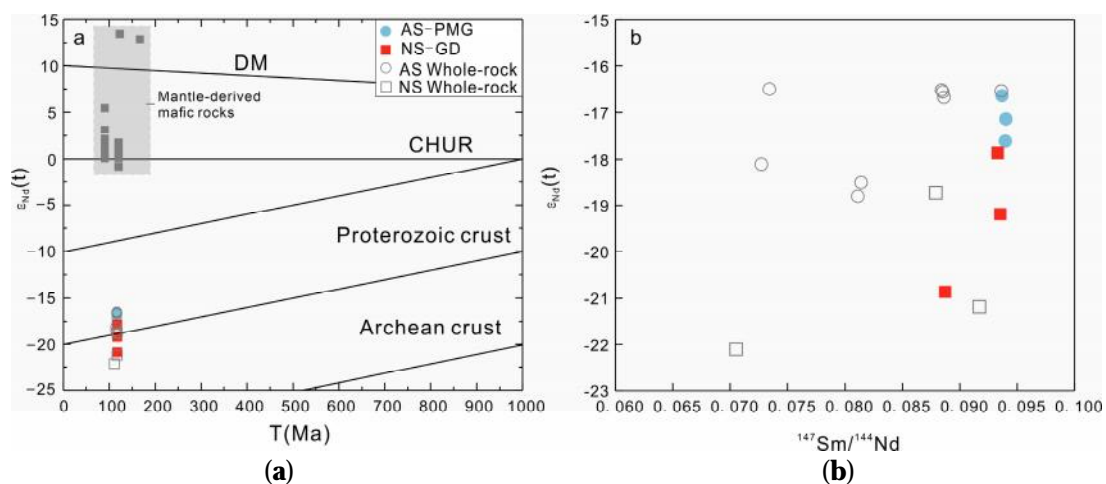
Figure 9. Binary diagram of $\varepsilon_{Nd}(t)$ vs. T (**a**) and $\varepsilon_{Nd}(t)$ vs. $^{147}Sm/^{144}Nd$ (**b**) in apatite from the Aishan pluton and Nansu pluton. AS-PMG: porphyritic medium-grained monzonitic granite of the ore-barren granitoid Aishan pluton; NS-GD: fine-grained granodiorite of the ore-fertile granitoid Nansu pluton; AS Whole-rock: Aishan pluton whole-rock Nd isotope data; NS Whole-rock: Nansu pluton whole-rock Nd isotope data (Whole-rock Nd isotope data from [67,70]; mantle-derived mafic rocks Nd isotope data from [72–74]).

Previous research and field geological observation of the Late Early Cretaceous granite in the Jiaodong Peninsula [60,67,98] proposed that mafic microgranular enclaves (MMEs) developed in both the Nansu and Aishan plutons. These MMEs have fine-grained structures and contain acicular apatite, suggesting that some mantle-derived mafic melts were added into the source of granitoids by magma mixing [59,99]. The average value of zircon δ^{18}O in the Nansu pluton is 6.62‰, which is closer to the depleted mantle value (5.3 ± 0.6‰) [60], suggesting that more mantle-derived materials might have been added to the magma source of the Nansu pluton.

5.3.2. Apatite Trace Element as Indicators of Magmatic Source

The binary diagrams plotting the ratios of Ba/Th, Sr/Th, and U/Th against La/Sm for apatite samples from the Aishan and Nansu plutons in the Jiaodong area demonstrate a prominent trend towards sediment melting in apatite samples originating from the Nansu pluton.

Labanieh et al. (2012) [100] conducted a study to evaluate the potential of La/Sm as a quantitative indicator for measuring the impact of volcanic arc sediments. Their research focused on Martinique Island, a unique geological location characterized by dehydration and sediment meltin [100]. Their findings revealed that the proportion of slab sediments incorporated into the mantle wedge plays a crucial role in determining the La/Sm ratio in the source region. Additionally, they delved into the relative significance of hydrous fluids in this process. The dehydration of the slab results in an elevation of Ba/Th, Sr/Th, and U/Th ratios in the lava, as Ba, Sr, and U preferentially partition into the aqueous phase. Conversely, Th can be effectively transferred from the slab only through the melting of sediments. Therefore, the ratio of fluid-mobile elements to Th serves as a reliable indicator for the occurrence of slab dehydration [101–106].

During the metamorphism of the subducted plate, fluids are released and metasomatize the mantle wedge, triggering partial melting. This process facilitates the enrichment of Ba, Sr, and U relative to Th, resulting in the formation of granitic magmas with elevated Ba/Th, Sr/Th, and U/Th ratios. The La/Sm ratio remains unaffected by partial melting and maintains relative stability in the magma. Instead, the La/Sm ratio is primarily controlled by the melting of subducted oceanic sediments. As the degree of sediment melting increases, the La/Sm ratio also rises. At the same time, the increasing sediment melting enhances the Th content, ensuring that the Ba/Th, Sr/Th, and U/Th ratio in the magma remain relatively stable [100,107]. Therefore, the melting of the sediments on the subducted slab would result in the elevated La/Sm ratio of the melt but stabilized Ba/Th, Sr/Th and U/Th ratio. However, the addition of the fluid released by the oceanic slab will have the opposite trend [100].

However, it is still uncertain whether the relationship between La/Sm ratio and Ba/Th, Sr/Th, U/Th ratio in the parental magma is inherited by apatite. Elements such as Sr, Th, U, and REEs are generally incorporated into apatite by isomorphic substitution. The content of these elements in apatite can reflect the contents of these elements in the parental magma [108]. The apatite-silicate melt partitioning experiments show that the La/Sm ratio of apatite is about 0.77 times that of the parental magma. Additionally, the Ba/Th, Sr/Th, and U/Th ratios of apatite are 0.2 times, 4.86 times, and 1.06 times those of the parent magma, respectively. These ratios are fixed values [77]. The results indicate that apatite does not significantly alter the trend of Ba/Th, Sr/Th, U/Th, and La/Sm ratios relative to the parent rock. Therefore, the Ba/Th, Sr/Th, U/Th, and La/Sm ratios of apatite can effectively distinguish between the two end members of sediment melting and slab dehydration products [109,110]. In Figure 10, the apatite grains from the Nansu pluton exhibit a distinct trend, suggestive of sediment melting. This result suggests that sedimentary materials may have been incorporated into the magmatic source of the Nansu ore-fertile granitoid, which contributed to the occurrence of molybdenum mineralization in the Nansu pluton.
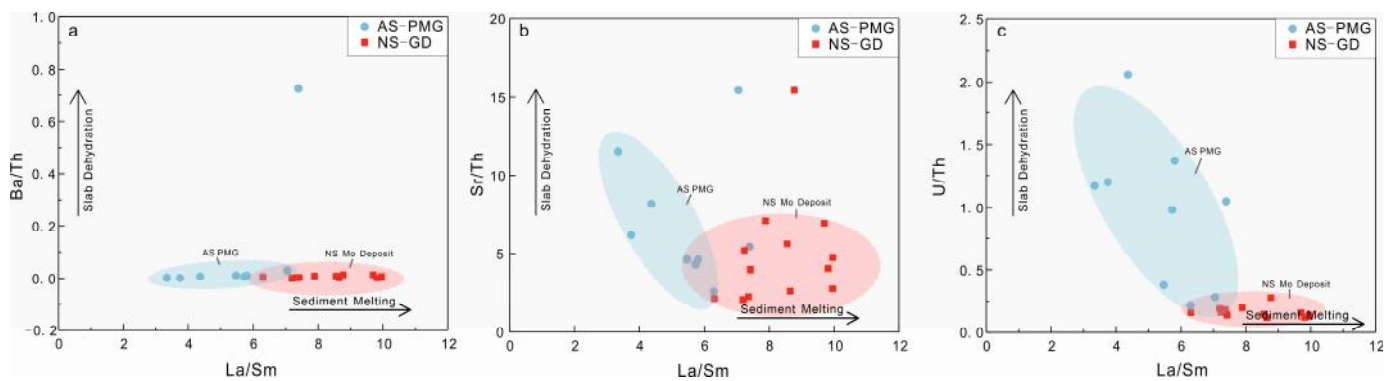
Figure 10. Binary diagram of Ba/Th vs. La/Sm (**a**), Sr/Th vs. La/Sm (**b**), and U/Th vs. La/Sm (**c**) in apatite from the Aishan pluton and Nansu pluton. The symbols are the same as in Figure 6.

The above discussion shows that the difference in magma source may be one of the most important reasons for the metallogenic difference between the Late Aptian Nansu and Aishan plutons in Jiaodong. In conclusion, much more mantle-derived materials suggested by lower apatite $\varepsilon_{Nd}(t)$ values and sedimentary materials indicated by higher apatite La/Sm ratios and lower apatite Sr/Th ratios involved in the magma source determined the Mo mineralized potential of Nansu pluton [100].

5.3.3. Possible Genesis of the Molybdenum Mineralization in the Nansu Pluton

The global distribution of porphyry molybdenum deposits is primarily concentrated within the Pacific metallogenic belt, and their genesis is intricately linked to plate subduction [111,112]. Mo is a moderately incompatible element with an abundance of 0.8×10^{-6} in the crust [113]. Simple magma formation and evolution processes make it difficult to directly enrich it from crustal abundance to industrial grade. Previous studies have shown that molybdenum mineralization primarily occurs through a two-stage enrichment process: one is the supergene process related to weathering and deposition; the second is the magmatic process related to plate subduction or deep burial melting [111,112]. After the second significant increase in atmospheric oxygen in the Cambrian molybdenum, as a variable valence element, becomes prone to oxidation, transforming into water-soluble MoO_4^{2-} during surface chemical weathering. This oxidized molybdenum is then transported by surface runoff into oceans and lakes, and under reducing conditions, it is deposited in black shale and other organic-rich sediments. Subsequently, these Mo-rich sediments can undergo partial melting due to heating and metamorphism under conditions of plate subduction to the mantle or deep burial. This process gives rise to molybdenum-rich parental magmas, ultimately leading to mineralization.

The Re-Os isotopic age of molybdenite in Nansu granite is 117.8 ± 7.0 Ma [63], indicating that the mineralization of molybdenite occurred concurrently with the formation of the Nansu pluton. A large number of studies have shown that the formation time of Au deposits in the Jiaodong Peninsula primarily occurred at ca. 120 Ma [44,47,54–57], indicating a general alignment between the timing of molybdenite mineralization and gold mineralization. Both processes occurred under the same tectonic background, and they exhibit close temporal, spatial, and genetic relationships. The study of sulfur isotope in the Jiaodong Au deposit shows that $\delta^{34}S$ is derived from the subducted oceanic plate and overlying sediments, which are the source and reservoir of gold and sulfur [114]. Au and S may be released during subduction, stored in the mantle wedge, and formed orogenic gold deposits through crustal uplift during lithospheric rollback [114]. Based on the evident sediment melting trend exhibited by apatite samples from the Nansu pluton in Figure 10, it is inferred that the molybdenum mineralization in the Nansu pluton may be genetically related to the recycling Mo-rich sediments in the reducing environment of water body through the supergene geochemical process after the Neoproterozoic oxidation event. These Mo-rich sediments, along with Au and S contained within the oceanic plate

and overlying sediments were released during the subduction of the Paleo–Pacific plate and stored in the mantle wedge. Subsequently, during tectonic transformation and/or asthenosphere upwelling caused by the Early Cretaceous extension, they were released by heating and rose through the crust during the lithosphere rollback [114,115]. Ultimately, they precipitated in the favorable structure of the upper crust.

6. Conclusions

The major and trace elements, as well as Nd isotopes, of magmatic apatite samples from both the Nansu pluton of molybdenum mineralization and ore-barren granitoid Aishan pluton of the late Aptian in the Jiaodong Peninsula, were comprehensively compared and analyzed. This comparison aimed to investigate the underlying causes of metallogenic differences between ore-fertile and ore-barren granitoids. The conclusions are as follows:

(1) The characteristics of major and trace elements of apatite show that the parental magma of ore-fertile and ore-barren granitoids both oxidize water-rich magma. Consequently, oxygen fugacity values and water contents of parental magma are not the reasons for the metallogenic difference between ore-fertile and ore-barren granitoids.

(2) The higher Ce/Pb ratio and relatively lower Th/U ratio of apatite in ore-fertile granitoid indicate that more fluids are involved in the process of magma evolution.

(3) The Nd isotope data of apatite in ore-fertile and ore-barren granitoids indicates that the magma may be Precambrian metamorphic basement rocks with a minor input of mantle-derived materials.

(4) The binary diagrams plotting the ratios of Ba/Th, Sr/Th, and U/Th against La/Sm for apatite reveal that a higher apatite La/Sm ratio and lower ratios of Ba/Th, Sr/Th, and U/Th suggest the involvement of sedimentary materials in the magma source. These sedimentary materials may include Mo-rich sediments, which contribute to the occurrence of molybdenum mineralization in the Nansu pluton. The difference in source area is one of the important reasons for the difference in mineralization in the late Early Cretaceous in Jiaodong.

Author Contributions: Conceptualization, L.Y. and K.L.; Writing—original draft, K.L.; Investigation, K.L. and L.J.; Software, K.L.; Data curation, K.L., L.J. and D.X.; Funding acquisition, L.Y.; Project administration, L.Y.; Supervision, L.Y.; Writing—review & editing, L.Y. All authors have read and agreed to the published version of the manuscript.

Data Availability Statement: Data are contained within the article.

Conflicts of Interest: Liqiang Yang is an employee of Institute of Geological Research, Shandong Gold Group Co., Ltd. The paper reflects the views of the scientists and not the company. Lei Ju is an employee of Kunlun Digital Technology Co., Ltd. The paper reflects the views of the scientists and not the company.

References

1. Summaries, M.C. *Mineral Commodity Summaries*; US Geological Survey: Reston, VA, USA, 2021.
2. Fan, Y.; Zhou, T.F.; Zhang, D.Y.; Yuan, F.; Ren, Z.; Noel, W. Spatial and Temporal Distribution and Metallogical Background of Chinese Molybdenum deposit. *Acta Geol. Sin.* **2014**, *88*, 784–804. [CrossRef]
3. Li, J.; Song, M.C.; Wang, M.Y.; Li, S.Y.; Zhou, M.L.; Ni, S.J.; Zhang, C.J.; Ding, Z.J.; Yue, Y.P. The molybdenite Re-Os age and genetic analysis of the Shangjiazhuang Mo deposit in Jiaodong area. *Geol. China* **2013**, *40*, 1612–1621.
4. Ding, Z.J.; Sun, F.Y.; Liu, F.L.; Liu, J.H.; Liu, D.H.; Zhang, P.J.; Du, S.X.; Li, B. U-Pb dating of zircons from the Weideshan molybdenum copper polymetallic deposits in Jiaodong Peninsula, China, and its geological significance. *Acta Petrol. Sin.* **2013**, *29*, 607–618.
5. Zou, J.; Li, Z.Q.; Liu, Z.; Fu, C.; Li, M.L.; Ma, F.; Zhao, X. Geological Characteristic and Origin Study on Xingjiashan Molybdenum Tungsten Deposit in Jiaodong Peninsula. *Shandong Land Resour.* **2020**, *36*, 1–9.
6. Zhu, B.L. *Geochemical Characteristics and Genetic Mechanism of the Kongxintou Fe-Cu-Mo skarn deposit in Jiaodong Metallogenic Area*; China University of Geosciences: Beijing, China, 2017.
7. Li, C.; Pei, H.X.; Wang, D.H.; Zhou, L.M.; Zhao, H.; Li, X.W.; Qu, W.J.; Du, A.D. Age and Source Constraints for Kongxintou Copper-Molybdenum Deposit Shandong from Re-Os Isotope in Molybdenite and Chalcopyrite. *Acta Geol. Sin.* **2016**, *90*, 240–249.
8. Cheng, S.B. *Contemporary Mineralization and Dynamic Mechanism of the Molybdenum and Gold Deposits in Jiaodong Metallogenic Area, Eastern China*; China University of Geosciences: Beijing, China, 2018.
9. Watson, E.B.; Capobianco, C.J. Phosphorus and the rare earth elements in felsic magmas: An assessment of the role of apatite. *Geochim. Cosmochim. Acta* **1981**, *45*, 2349–2358. [CrossRef]
10. Piccoli, P.M.; Candela, P.A. Apatite in felsic rocks; a model for the estimation of initial halogen concentrations in the Bishop Tuff (Long Valley) and Tuolumne Intrusive Suite (Sierra Nevada Batholith) magmas. *Rev. Mineral. Geochem.* **1994**, *294*, 92–135. [CrossRef]
11. Piccoli, P.M.; Candela, P.A. Apatite in Igneous Systems. *Rev. Mineral. Geochem.* **2002**, *48*, 255–292. [CrossRef]
12. Brassinnes, S.; Balaganskaya, E.; Demaiffe, D. Magmatic evolution of the differentiated ultramafic, alkaline and carbonatite intrusion of Vuoriyarvi (Kola Peninsula, Russia). A LA-ICP-MS study of apatite. *Lithos* **2005**, *85*, 76–92. [CrossRef]
13. Hsieh, P.S.; Chen, C.H.; Yang, H.J.; Lee, C.Y. Petrogenesis of the Nanling Mountains granites from South China: Constraints from systematic apatite geochemistry and whole-rock geochemical and Sr–Nd isotope compositions. *J. Asian Earth Sci.* **2008**, *33*, 428–451. [CrossRef]
14. Spear, F.S.; Pyle, J.M. Apatite, Monazite, and Xenotime in Metamorphic Rocks. *Rev. Mineral. Geochem.* **2002**, *48*, 293–335. [CrossRef]
15. O'Sullivan, G.J.; Chew, D.M.; Samson, S.D. Detecting magma-poor orogens in the detrital record. *Geology* **2016**, *44*, 871–874. [CrossRef]
16. Henrichs, I.A.; O'Sullivan, G.; Chew, D.M.; Mark, C.; Babechuk, M.G.; McKenna, C.; Emo, R. The trace element and U-Pb systematics of metamorphic apatite. *Chem. Geol.* **2018**, *483*, 218–238. [CrossRef]
17. Belousova, E.A.; Griffin, W.L.; O'Reilly, S.Y.; Fisher, N.I. Apatite as an indicator mineral for mineral exploration: Trace-tlement compositions and their relationship to host rock type. *J. Geochem. Explor.* **2002**, *76*, 45–69. [CrossRef]
18. Bouzari, F.; Hart, C.J.R.; Bissig, T.; Barker, S. Hydrothermal Alteration Revealed by Apatite Luminescence and Chemistry: A Potential Indicator Mineral for Exploring Covered Porphyry Copper Deposits. *Econ. Geol.* **2016**, *111*, 1397–1410. [CrossRef]
19. Mao, M.; Rukhlov, A.S.; Rowins, S.M.; Spence, J.; Coogan, L.A. Apatite Trace Element Compositions: A Robust New Tool for Mineral Exploration. *Econ. Geol.* **2016**, *111*, 1187–1222. [CrossRef]
20. Sha, L.K.; Chappell, B.W. Apatite Chemical Composition, Determined by Electron Microprobe and Laser-Ablation Inductively Coupled Plasma Mass Spectrometry, as a Probe into Granite Petrogenesis. *Geochem. Cosmochim. Acta* **1999**, *63*, 3861–3881. [CrossRef]
21. Belousova, E.A.; Walters, S.W.; Griffin, W.L.; O'Reilly, S.Y. Trace-element signatures of apatites in granitoids from the Mt Isa Inlier, northwestern Queensland. *Aust. J. Earth Sci.* **2001**, *48*, 603–619. [CrossRef]
22. Boyce, J.W.; Hervig, R.L. Apatite as a monitor of late-stage magmatic processes at Volcán Irazú, Costa Rica. *Contrib. Mineral. Petrol.* **2009**, *157*, 135–145. [CrossRef]
23. Boyce, J.W.; Liu, Y.; Rossman, G.R.; Guan, Y.; Eiler, J.M.; Stolper, E.M.; Taylor, L.A. Lunar apatite with terrestrial volatile abundances. *Nature* **2010**, *466*, 466–469. [CrossRef]
24. Elkins-Tanton, L.T.; Grove, T.L. Water (hydrogen) in the lunar mantle: Results from petrology and magma ocean modeling. *Earth Planet. Sci. Lett.* **2011**, *307*, 173–179. [CrossRef]
25. Jennings, E.S.; Marschall, H.R.; Hawkesworth, C.J.; Storey, C.D. Characterization of magma from inclusions in zircon: Apatite and biotite work well, feldspar less so. *Geology* **2011**, *39*, 863–866. [CrossRef]
26. Schisa, P.; Boudreau, A.; Djon, L.; Tchalikian, A.; Corkery, J. The Lac Des Iles Palladium Deposit, Ontario, Canada. Part II. Halogen variations in apatite. *Miner. Depos.* **2015**, *50*, 339–355. [CrossRef]
27. Webster, J.D.; Piccoli, P.M. Magmatic Apatite: A Powerful, Yet Deceptive, Mineral. *Elements* **2015**, *11*, 177–182. [CrossRef]
28. Cao, M.J.; Li, G.M.; Qin, K.Z.; Seitmuratova, E.Y.; Liu, Y.S. Major and Trace Element Characteristics of Apatites in Granitoids from Central Kazakhstan: Implications for Petrogenesis and Mineralization. *Resour. Geol.* **2011**, *62*, 63–83. [CrossRef]

29. Miles, A.J.; Graham, C.M.; Hawkesworth, C.J.; Gillespie, M.R.; Hinton, R.W.; Bromiley, G.D. Apatite: A new redox proxy for silicic magmas? *Geochim. Cosmochim. Acta* **2014**, *132*, 101–119. [CrossRef]

30. Bruand, E.; Storey, C.; Fowler, M. Accessory Mineral Chemistry of High Ba–Sr Granites from Northern Scotland: Constraints on Petrogenesis and Records of Whole-rock Signature. *J. Petrol.* **2014**, *55*, 1619–1651. [CrossRef]

31. Bruand, E.; Storey, C.; Fowler, M. An apatite for progress: Inclusions in zircon and titanite constrain petrogenesis and provenance. *Geology* **2016**, *44*, 91–94. [CrossRef]

32. Bruand, E.; Fowler, M.; Storey, C.; Darling, J. Apatite trace element and isotope applications to petrogenesis and provenance. *Am. Min.* **2017**, *102*, 75–84. [CrossRef]

33. Ji, D.; Dygert, N. Trace element partitioning between apatite and silicate melts: Effects of major element composition, temperature, and oxygen fugacity, and implications for the volatile element budget of the lunar magma ocean. *Geochim. Cosmochim. Acta* **2024**, *369*, 141–159. [CrossRef]

34. Deng, J.; Gong, Q.J.; Wang, C.M.; Carranza, E.J.M.; Santosh, M. Sequence of Late Jurassic–Early Cretaceous magmatic–hydrothermal events in the Xiong'ershan region, Central China: An overview with new zircon U–Pb geochronology data on quartz porphyries. *J. Asian Earth Sci.* **2014**, *79*, 161–172. [CrossRef]

35. Deng, J.; Liu, X.F.; Wang, Q.F.; Pan, R.G. Origin of the Jiaodong-type Xinli gold deposit, Jiaodong Peninsula, China: Constraints from fluid inclusion and C–D–O–S–Sr isotope compositions. *Ore Geol. Rev.* **2015**, *65*, 674–686. [CrossRef]

36. Huang, J.; Zheng, Y.F.; Zhao, Z.F.; Wu, Y.B.; Zhou, J.B.; Liu, X.M. Melting of subducted continent: Element and isotopic evidence for a genetic relationship between Neoproterozoic and Mesozoic granitoids in the Sulu orogen. *Chem. Geol.* **2006**, *229*, 227–256. [CrossRef]

37. Zhang, J.; Zhao, Z.F.; Zheng, Y.F.; Liu, X.M.; Xie, L.W. Zircon Hf–O isotope and whole-rock geochemical constraints on origin of postcollisional mafic to felsic dykes in the Sulu orogen. *Lithos* **2012**, *136–139*, 225–245. [CrossRef]

38. Zheng, J.P.; Sun, M.; Lu, F.X.; Pearson, N. Mesozoic lower crustal xenoliths and their significance in lithospheric evolution beneath the Sino-Korean Craton. *Tectonophysics* **2003**, *361*, 37–60. [CrossRef]

39. Deng, J.; Wang, Q.F.; Xiao, C.H.; Yang, L.Q.; Liu, H.; Gong, Q.J.; Zhang, J. Tectonic-magmatic-metallogenic system, Tongling ore cluster region, Anhui Province, China. *Int. Geol. Rev.* **2011**, *53*, 449–476. [CrossRef]

40. Yang, L.Q.; Deng, J.; Guo, C.Y.; Zhang, J.; Jiang, S.Q.; Gao, B.F.; Gong, Q.J.; Wang, Q.F. Ore-Forming Fluid Characteristics of the Dayingezhuang Gold Deposit, Jiaodong Gold Province, China. *Resour. Geol.* **2009**, *59*, 181–193. [CrossRef]

41. Yang, L.Q.; Deng, J.; Wang, Z.L.; Zhang, L.; Goldfarb, R.J.; Yuan, W.M.; Weinberg, R.F.; Zhang, R.-Z. Thermochronologic constraints on evolution of the Linglong Metamorphic Core Complex and implications for gold mineralization: A case study from the Xiadian gold deposit, Jiaodong Peninsula, eastern China. *Ore Geol. Rev.* **2016**, *72*, 165–178. [CrossRef]

42. Yang, L.Q.; Deng, J.; Wang, Z.L.; Guo, L.N.; Li, R.H.; Groves, D.I.; Danyushevsky, L.V.; Zhang, C.; Zheng, X.L.; Zhao, H. Relationships Between Gold and Pyrite at the Xincheng Gold Deposit, Jiaodong Peninsula, China: Implications for Gold Source and Deposition in a Brittle Epizonal Environment. *Econ. Geol.* **2016**, *111*, 105–126. [CrossRef]

43. Yang, L.Q.; Deng, J.; Wang, Z.L.; Zhang, L.; Guo, L.N.; Song, M.C.; Zheng, X.L. Mesozoic gold metallogenic system of the Jiaodong gold province, eastern China. *Acta Petrol. Sin.* **2014**, *30*, 2447–2467.

44. Deng, J.; Qiu, K.F.; Wang, Q.F.; Goldfarb, R.; Yang, L.Q.; Zi, J.W.; Geng, J.Z.; Ma, Y. In situ dating of hydrothermal monazite and implications for the geodynamic controls on ore formation in the jiaodong gold province, eastern china. *Econ. Geol.* **2020**, *115*, 671–685. [CrossRef]

45. Yang, L.Q.; Deng, J.; Ge, L.S.; Wang, Q.F.; Zhang, J.; Gao, B.F.; Jiang, S.Q.; Xu, H. Metallogenic epoch and genesis of the gold deposits in Jiaodong Peninsula, Eastern China: A regional review. *Prog. Nat. Sci.* **2007**, *17*, 138–143.

46. Wang, L.M.; Ren, T.L.; Liu, H.D.; Ning, Z.G.; Yu, X.W.; Guo, R.M.; Hou, J.H.; Zhu, X.Q. Division of Mesozoic Granites in Jiaodong Area. *Shandong Land Resour.* **2021**, *37*, 1–14.

47. Yang, L.Q.; Deng, J.; Goldfarb, R.J.; Zhang, J.; Gao, B.F.; Wang, Z.L. 40Ar/39Ar geochronological constraints on the formation of the Dayingezhuang gold deposit: New implications for timing and duration of hydrothermal activity in the Jiaodong gold province, China. *Gondwana Res.* **2014**, *25*, 1469–1483. [CrossRef]

48. Chen, J.F.; Xie, Z.D.; Li, H.M.; Zhang, X.D.; Zhou, T.X.; Park, Y.S.; Ahn, K.; Chen, D.G.; Zhang, X. U-Pb zircon ages for a collision-related K-rich complex at Shidao in the Sulu ultrahigh pressure terrane, China. *Geochem. J.* **2003**, *37*, 35–46. [CrossRef]

49. Wang, L.G.; Qiu, Y.; McNaughton, N.J.; Groves, D.I.; Luo, Z.-H.; Huang, J.Z.; Miao, L.; Liu, Y. Constraints on crustal evolution and gold metallogeny in the Northwestern Jiaodong Peninsula, China, from SHRIMP U–Pb zircon studies of granitoids. *Ore Geol. Rev.* **1998**, *13*, 275–291. [CrossRef]

50. Wang, Z.L.; Yang, L.Q.; Deng, J.; Santosh, M.; Zhang, H.F.; Liu, Y.; Li, R.H.; Huang, T.; Zheng, X.L.; Zhao, H.B. Gold-hosting high Ba-Sr granitoids in the Xincheng gold deposit, Jiaodong Peninsula, East China: Petrogenesis and tectonic setting. *J. Asian Earth Sci.* **2014**, *95*, 274–299. [CrossRef]

51. Guo, J.H.; Chen, F.K.; Zhang, X.M.; Siebel, W.; Zhai, M.G. Evolution of syn- to post-collisional magmatism from north Sulu UHP belt, eastern China: Zircon U-Pb geochronology. *Acta Petrol. Sin.* **2005**, *21*, 1281–1301.

52. Wang, Y.J.; Fan, W.M.; Zhang, G.W.; Zhang, Y.H. Phanerozoic tectonics of the South China Block: Key observations and controversies. *Gondwana Res.* **2013**, *23*, 1273–1305. [CrossRef]

53. Yang, L.Q.; Deng, J.; Groves, D.I.; Santosh, M.; He, W.Y.; Li, N.; Zhang, L.; Zhang, R.X.; Zhang, H.R. Metallogenic 'factories' and resultant highly anomalous mineral endowment on the craton margins of China. *Geosci. Front.* **2022**, *13*, 101339. [CrossRef]

54. Li, J.W.; Vasconcelos, P.M.; Zhang, J.; Zhou, M.F.; Zhang, X.J.; Yang, F.H. 40Ar/39Ar Constraints on a Temporal Link between Gold Mineralization, Magmatism, and Continental Margin Transtension in the Jiaodong Gold Province, Eastern China. *J. Geol.* **2003**, *111*, 741–751. [CrossRef]

55. Li, J.W.; Paulo, V.; Zhou, M.F.; Zhao, X.F.; Ma, C.Q. Geochronology of the Pengjiakuang and Rushan Gold Deposits, Eastern Jiaodong Gold Province, Northeastern China: Implications for Regional Mineralization and Geodynamic Setting. *Econ. Geol.* **2006**, *101*, 1023–1038. [CrossRef]

56. Li, Q.L.; Chen, F.K.; Yang, J.H.; Fan, H.R. Single grain pyrite Rb–Sr dating of the Linglong gold deposit, eastern China. *Ore Geol. Rev.* **2008**, *34*, 263–270. [CrossRef]

57. Zhang, L.; Weinberg, R.F.; Yang, L.-Q.; Groves, D.I.; Sai, S.-X.; Matchan, E.; Phillips, D.; Kohn, B.P.; Miggins, D.P.; Liu, Y.; et al. Mesozoic Orogenic Gold Mineralization in the Jiaodong Peninsula, China: A Focused Event at 120 ± 2 Ma During Cooling of Pregold Granite Intrusions. *Econ. Geol.* **2020**, *115*, 415–441. [CrossRef]

58. Ding, Z.J.; Sun, F.; Liu, F.L.; Liu, J.H.; Peng, Q.M.; Ji, P.; Li, B.L.; Zhang, P.J. Mesozoic geodynamic evolution and metallogenic series of major metal deposits in Jiaodong Peninsula, China. *Acta Petrol. Sin.* **2015**, *31*, 3045–3080.

59. Cheng, S.B.; Liu, Z.J.; Wang, Q.F.; Wang, F.J.; Xue, Y.S.; Xu, L.; Wang, J.P.; Zhu, B.L. Mineralization age and geodynamic background for the Shangjiazhuang Mo deposit in the Jiaodong gold province, China. *Ore Geol. Rev.* **2017**, *80*, 876–890. [CrossRef]

60. Cheng, S.B.; Lü, Q.T.; Liu, Z.J.; Yang, Y.; Liu, Z.D.; Yan, J.Y.; Zhang, H.; Gong, X.J.; Chen, C.X. Petrogenesis of Mo-associated Mesozoic granitoids on the Jiaodong Peninsula: Implications for crustal architecture and Mo mineralization along the Dabie–Sulu Orogen. *Ore Geol. Rev.* **2022**, *149*, 105015. [CrossRef]

61. Zhao, L.H. Types of Molybdenum Ore Deposits in the Eastern Shandong Region and its Characteristics of Minerlization. *Shandong Geol.* **1998**, *4*, 101–112.

62. Ding, Z.J.; Sun, F.Y.; Liu, J.H.; Liu, D.H.; Li, B.L.; Zhang, P.J.; Qian, Y.; Li, J. Re-Os dating of molybdenites from the Xingjiashan molybdenum-tungsten deposit in Jiaodong Peninsula, China and its geological significance. *Acta Petrol. Sin.* **2012**, *28*, 2721–2732.

63. Liu, Z.-J.; Wang, J.-P.; Liu, J.-J.; Fu, C. The molybdenite Re-Os isotopic ages of Nansu granite and its significance, Jiaodong Peninsula. *Miner. Depos.* **2010**, *29*, 483–484. [CrossRef]

64. Ma, W.D.; Fan, H.R.; Liu, X.; Pirajno, F.; Hu, F.F.; Yang, K.F.; Yang, Y.H.; Xu, W.G.; Jiang, P. Geochronological framework of the Xiadian gold deposit in the Jiaodong province, China: Implications for the timing of gold mineralization. *Ore Geol. Rev.* **2017**, *86*, 196–211. [CrossRef]

65. Wen, B.J.; Fan, H.R.; Hu, F.F.; Yang, K.F.; Liu, X.; Cai, Y.C.; Sun, Z.F.; Sun, Z.F. The genesis of pegmatite-type molybdenum mineralization in Sanshandao, and their implications for molybdenum deposit in Jiaodong. *East China Acta Petrol. Sin.* **2015**, *31*, 1002–1014.

66. Zhu, B.L.; Liu, Z.J.; Cheng, S.B.; Xue, Y.S.; Wang, J.P.; Xu, L. Re-Os isotopic dating of molybdenites from the Yuangezhuang pluton in Jiaodong and its geolgcial significance. *Geol. China* **2016**, *43*, 1353–1366. [CrossRef]

67. Song, M.; Zhou, J.B.; Song, Y.X.; Wang, B.; Li, S.Y.; Li, J.; Wang, S.S. Mesozoic Weideshan granitoid suite and its relationship to large-scale gold mineralization in the Jiaodong Peninsula, China. *Geol. J.* **2020**, *55*, 5703–5724. [CrossRef]

68. Yang, Y.H.; Wu, F.Y.; Yang, J.H.; Chew, D.M.; Xie, L.W.; Chu, Z.Y.; Zhang, Y.B.; Huang, C. Sr and Nd isotopic compositions of apatite reference materials used in U–Th–Pb geochronology. *Chem. Geol.* **2014**, *385*, 35–55. [CrossRef]

69. Ketcham, R.A. Technical Note: Calculation of stoichiometry from EMP data for apatite and other phases with mixing on monovalent anion sites. *Am. Min.* **2015**, *100*, 1620–1623. [CrossRef]

70. Ju, L. *Ore-Forming Factors of Late Early Cretaceous Porphyry-Skarn-Type Molybdenum-Copper Deposits in Jiaodong*; China University of Geosciences: Beijing, China, 2023.

71. Sun, S.S.; McDonough, W.F. Chemical and isotopic systematics of oceanic basalts: Implications for mantle composition and processes. *Geol. Soc. Lond. Spec. Publ.* **1989**, *42*, 313–345. [CrossRef]

72. Ma, L.; Jiang, S.Y.; Hofmann, A.W.; Dai, B.Z.; Hou, M.Q.; Zhao, K.D.; Chen, L.H.; Li, J.W.; Jiang, Y.H. Lithospheric and asthenospheric sources of lamprophyres in the Jiaodong Peninsula: A consequence of rapid lithospheric thinning beneath the North China Craton? *Geochim. Cosmochim. Acta* **2014**, *124*, 250–271. [CrossRef]

73. Cai, Y.C.; Fan, H.R.; Santosh, M.; Liu, X.; Hu, F.F.; Yang, K.F.; Lan, T.G.; Yang, Y.H.; Liu, Y.S. Evolution of the lithospheric mantle beneath the southeastern North China Craton:Constraints from mafic dikes in the Jiaobei terrain. *Gondwana Res.* **2013**, *24*, 601–621. [CrossRef]

74. Sun, J.G.; Hu, S.X.; Liu, J.M.; Shen, K.; Ling, H.F. A Study of Sr, Nd and O Isotopes of the K-rich Melanocratic Dykes in the Late Mesozoic Gold Field in the Jiaodong Peninsula. *Acta Geol. Sin.-Engl.* **2010**, *75*, 432–444. [CrossRef]

75. Ouyang, H.G. Controlling factors on the formation of porphyry-skarn Mo deposits. *Bull. Mineral. Petrol. Geochem.* **2023**, *43*, 1–12. [CrossRef]

76. Streck, M.J.; Dilles, J.H. Sulfur evolution of oxidized arc magmas as recorded in apatite from a porphyry copper batholith. *Geology* **1998**, *26*, 523–526. [CrossRef]

77. Prowatke, S.; Klemme, S. Trace element partitioning between apatite and silicate melts. *Geochim. Cosmochim. Acta* **2006**, *70*, 4513–4527. [CrossRef]

78. Chen, L.; Zhang, Y. In situ major-, trace-elements and Sr-Nd isotopic compositions of apatite from the Luming porphyry Mo deposit, NE China: Constraints on the petrogenetic-metallogenic features. *Ore Geol. Rev.* **2018**, *94*, 93–103. [CrossRef]

79. Pan, L.C.; Hu, R.Z.; Wang, X.S.; Bi, X.W.; Zhu, J.J.; Li, C.S. Apatite trace element and halogen compositions as petrogenetic-metallogenic indicators: Examples from four granite plutons in the Sanjiang region, SW China. *Lithos* **2016**, *254–255*, 118–130. [CrossRef]

80. Ridolfi, F. Amp-TB2: An Updated Model for Calcic Amphibole Thermobarometry. *Minerals* **2021**, *11*, 324. [CrossRef]

81. Yang, Y.; Wang, X.X.; Yu, X.W.; Ke, C.H.; Wang, L.G.; Guo, R.P.; Wang, S.A.; Li, X.X. Chemical composition of biotite and amphibole from Mesozoic granites in northwestern Jiaodong Peninsula, China and their implications. *Acta Petrol. Sin.* **2017**, *33*, 3123–3136.

82. Mathez, E.A.; Webster, J.D. Partitioning behavior of chlorine and fluorine in the system apatite-silicate melt-fluid. *Geochim. Cosmochim. Acta* **2005**, *69*, 1275–1286. [CrossRef]

83. Hu, S.; Lin, Y.; Zhang, J.; Hao, J.; Feng, L.; Xu, L.; Yang, W.; Yang, J. NanoSIMS analyses of apatite and melt inclusions in the GRV 020090 Martian meteorite: Hydrogen isotope evidence for recent past underground hydrothermal activity on Mars. *Geochim. Cosmochim. Acta* **2014**, *140*, 321–333. [CrossRef]

84. McCubbin, F.M.; Steele, A.; Nekvasil, H.; Schnieders, A.; Rose, T.; Fries, M.; Carpenter, P.K.; Jolliff, B.L. Detection of structurally bound hydroxyl in fluorapatite from Apollo Mare basalt 15058,128 using TOF-SIMS. *Am. Min.* **2010**, *95*, 1141–1150. [CrossRef]

85. Tartèse, R.; Anand, M.; Barnes, J.J.; Starkey, N.A.; Franchi, I.A.; Sano, Y. The abundance, distribution, and isotopic composition of Hydrogen in the Moon as revealed by basaltic lunar samples: Implications for the volatile inventory of the Moon. *Geochim. Cosmochim. Acta* **2013**, *122*, 58–74. [CrossRef]

86. Robinson, K.L.; Taylor, G.J. Heterogeneous distribution of water in the Moon. *Nat. Geosci.* **2014**, *7*, 401–408. [CrossRef]

87. McCubbin, F.M.; Hauri, E.H.; Elardo, S.M.; Vander Kaaden, K.E.; Wang, J.; Shearer, C.K. Hydrous melting of the martian mantle produced both depleted and enriched shergottites. *Geology* **2012**, *40*, 683–686. [CrossRef]

88. McCubbin, F.M.; Kaaden, K.E.V.; Tartèse, R.; Klima, R.L.; Liu, Y.; Mortimer, J.; Barnes, J.J.; Shearer, C.; Treiman, A.H.; Lawrence, D.J.; et al. Magmatic volatiles (H, C, N, F, S, Cl) in the lunar mantle, crust, and regolith: Abundances, distributions, processes, and reservoirs. *Am. Min.* **2015**, *100*, 1668–1707. [CrossRef]

89. Qiu, K.F.; Zhou, T.; Chew, D.; Hou, Z.L.; Müller, A.; Yu, H.C.; Lee, R.G.; Chen, H.; Deng, J. Apatite trace element composition as an indicator of ore deposit types: A machine learning approach. *Am. Min.* **2024**, *109*, 303–314. [CrossRef]

90. Shannon, R.D. Revised effective ionic radii and systematic studies of interatomic distances in halides and chalcogenides. *Acta Cryst. A* **1976**, *32*, 751–767. [CrossRef]

91. Greenland, L.P.; Lovering, J.F. Fractionation of fluorine, chlorine and other trace elements during differentiation of a tholeiitic magma. *Geochim. Cosmochim. Acta* **1966**, *30*, 963–982. [CrossRef]

92. Sun, C.Y.; Cawood, P.A.; Xu, W.L.; Zhang, X.M.; Tang, J.; Li, Y.; Sun, Z.B.; Xu, T. In situ geochemical composition of apatite in granitoids from the eastern Central Asian Orogenic Belt: A window into petrogenesis. *Geochim. Cosmochim. Acta* **2021**, *317*, 552–573. [CrossRef]

93. Kogiso, T.; Tatsumi, Y.; Nakano, S. Trace element transport during dehydration processes in the subducted oceanic crust: 1. Experiments and implications for the origin of ocean island basalts. *Earth Planet. Sci. Lett.* **1997**, *148*, 193–205. [CrossRef]

94. Sun, J.F.; Yang, J.H.; Wu, F.Y.; Li, X.H.; Yang, Y.H.; Xie, L.W.; Wilde, S.A. Magma mixing controlling the origin of the Early Cretaceous Fangshan granitic pluton, North China Craton: In situ U-Pb age and Sr-, Nd-, Hf- and O-isotope evidence. *Lithos* **2010**, *120*, 421–438. [CrossRef]

95. Sun, J.F.; Zhang, J.H.; Yang, J.H.; Yang, Y.H.; Chen, S. Tracing magma mixing and crystal–melt segregation in the genesis of syenite with mafic enclaves: Evidence from in situ zircon Hf–O and apatite Sr–Nd isotopes. *Lithos* **2019**, *334–335*, 42–57. [CrossRef]

96. Sun, J.F.; Yang, J.H.; Zhang, J.H.; Yang, Y.H.; Zhu, Y.S. Apatite geochemical and Sr Nd isotopic insights into granitoid petrogenesis. *Chem. Geol.* **2021**, *566*, 120104. [CrossRef]

97. Qu, P.; Yang, W.B.; Niu, H.C.; Li, N.B.; Wu, D. Apatite fingerprints on the magmatic-hydrothermal evolution of the Daheishan giant porphyry Mo deposit, NE China. *GSA Bull.* **2021**, *134*, 1863–1876. [CrossRef]

98. Wang, B.; Zhou, J.B.; Ding, Z.J.; Wilde, S.A.; Song, M.C.; Zhao, T.Q.; Bao, Z.Y. Late Mesozoic magmatism and gold metallogeny of the Jiaodong Peninsula, China: A response to the destruction of the North China Craton. *GSA Bull.* **2023**, *136*, 1395–1412. [CrossRef]

99. Li, X.C.; Fan, H.R.; Santosh, M.; Hu, F.F.; Yang, K.F.; Lan, T.G.; Liu, Y.S.; Yang, Y.H. An evolving magma chamber within extending lithosphere: An integrated geochemical, isotopic and zircon U-Pb geochronological study of the Gushan granite, eastern North China Craton. *Prog. Nat. Sci.* **2012**, *50*, 27–43. [CrossRef]

100. Labanieh, S.; Chauvel, C.; Germa, A.; Quidelleur, X. Martinique: A Clear Case for Sediment Melting and Slab Dehydration as a Function of Distance to the Trench. *J. Petrol.* **2012**, *53*, 2441–2464. [CrossRef]

101. Condomines, M.; Hemond, C.A.M.; Allègre, C.J. U-Th-Ra radioactive disequilibria and magmatic processes. *Earth Planet. Sci. Lett.* **1988**, *90*, 243–262. [CrossRef]

102. McDermott, F.; Hawkesworth, C.J. Th, Pb, and Sr isotope variations in young island arc volcanics and oceanic sediments. *Earth Planet. Sci. Lett.* **1991**, *104*, 1–15. [CrossRef]

103. Gill, J.B.; Condomines, M. Short-Lived Radioactivity and Magma Genesis. *Science* **1992**, *257*, 1368–1376. [CrossRef]

104. Hawkesworth, C.J.; Turner, S.P.; McDermott, F.; Peate, D.W.; van Calsteren, P. U-Th Isotopes in Arc Magmas: Implications for Element Transfer from the Subducted Crust. *Science* **1997**, *276*, 551–555. [CrossRef]

105. Johnson, M.C.; Plank, T. Dehydration and melting experiments constrain the fate of subducted sediments. *Geochem. Geophys.* **1999**, *1*, 1–26. [CrossRef]

106. Plank, T.A. Constraints from Thorium/Lanthanum on Sediment Recycling at Subduction Zones and the Evolution of the Continents. *J. Petrol.* **2005**, *46*, 921–944. [CrossRef]

107. Turner, S.; Foden, J. U, Th and Ra disequilibria, Sr, Nd and Pb isotope and trace element variations in Sunda arc lavas: Predominance of a subducted sediment component. *Contrib. Mineral. Petrol.* **2001**, *142*, 43–57. [CrossRef]

108. Chu, M.F.; Wang, K.L.; Griffin, W.L.; Chung, S.L.; O'Reilly, S.Y.; Pearson, N.J.; Iizuka, Y. Apatite Composition: Tracing Petrogenetic Processes in Transhimalayan Granitoids. *J. Petrol.* **2009**, *50*, 1829–1855. [CrossRef]

109. Ding, T.; Ma, D.S.; Lu, J.J.; Zhang, R.Q. Apatite in granitoids related to polymetallic mineral deposits in southeastern Hunan Province, Shi–Hang zone, China: Implications for petrogenesis and metallogenesis. *Ore Geol. Rev.* **2015**, *69*, 104–117. [CrossRef]

110. Zafar, T.; Rehman, H.U.; Mahar, M.A.; Alam, M.; Oyebamiji, A.; Rehman, S.U.; Leng, C.B. A critical review on petrogenetic, metallogenic and geodynamic implications of granitic rocks exposed in north and east China: New insights from apatite geochemistry. *J. Geodyn.* **2020**, *136*, 101723. [CrossRef]

111. Sun, W.D.; Li, C.Y.; Ling, M.X.; Ding, X.; Yang, X.Y.; Liang, H.Y.; Zhang, H.; Fan, W.M. The geochemical behavior of molybdnum and mineralization. *Acta Petrol. Sin.* **2015**, *31*, 1807–1817.

112. Li, C.Y.; Liao, R.Q. Formation mechanism and geochemical process of porphyry molybdenum deposits. *Acta Petrol. Sin.* **2020**, *36*, 77–84.

113. Rudnick, R.L.; Gao, S. Composition of the Continental Crust. *Treatise Geochem.* **2014**, *4*, 1–51.

114. Qiu, K.F.; Deng, J.; Laflamme, C.; Long, Z.Y.; Wan, R.Q.; Moynier, F.; Yu, H.C.; Zhang, J.Y.; Ding, Z.J.; Goldfarb, R. Giant Mesozoic gold ores derived from subducted oceanic slab and overlying sediments. *Geochim. Cosmochim. Acta* **2023**, *343*, 133–141. [CrossRef]

115. Wu, F.Y.; Yang, J.H.; Xu, Y.G.; Wilde, S.A.; Walker, R.J. Destruction of the North China Craton in the Mesozoic. *Annu. Rev. Earth Planet. Sci.* **2019**, *47*, 173–195. [CrossRef]